Journal of MATERIALS RESEARCH

Review
DOI: 10.1557/jmr.2019.37

This section of Journal of Materials Research is reserved for papers that are reviews of literature in a given area.

NANOCRYSTALLINE HIGH ENTROPY MATERIALS: PROCESSING CHALLENGES AND PROPERTIES

FOCUS ISSUE

High-entropy alloys by mechanical alloying: A review

Mayur Vaidya[1], Garlapati Mohan Muralikrishna[1], Budaraju Srinivasa Murty[1,a)]

[1]*Department of Metallurgical and Materials Engineering, Indian Institute of Technology Madras, Chennai 600036, India*
[a)]Address all correspondence to this author. e-mail: murty@iitm.ac.in

Received: 6 September 2018; accepted: 23 January 2019

Mechanical alloying (MA) followed by sintering has been one of the most widely adopted routes to produce nanocrystalline high-entropy alloys (HEAs). Enhanced solid solubility, room temperature processing, and homogenous alloy formation are the key benefits provided by MA. Spark plasma sintering has largely been used to obtain high-density HEA pellets from milled powders. However, there are many challenges associated with the production of HEAs using MA, which include contamination during milling and high propensity of oxidation. The present review provides a comprehensive understanding of various HEAs produced by MA so far, with the aim to bring out the governing aspects of phase evolution, thermal stability, and properties achieved. The limitations and challenges of the process are also critically assessed with a possible way forward. The paper also compares the results obtained from high-pressure torsion, another severe plastic deformation technique.

Introduction

Materials development has always been at the forefront of technological innovations, which have governed the growth of human civilizations since ancient times. Alloys have been an integral part of materials evolution, since their first accidental discovery (arsenic bronze, 3000 BCE) in the primeval cave fires [1]. The conventional alloy design strategy involved adding one or more elements to a parent metal to achieve enhancement in desired properties. A plethora of currently used alloys, like steels, bronzes, aluminum alloys, and magnesium alloys, were developed using this traditional approach. It followed that the exploration of phase diagrams was largely limited to three dimensions and terminal composition range. However, a shift in this paradigm occurred more than a decade ago when parallel works of Cantor et al. [2] and Yeh et al. [3] marked the beginning of a new class of multicomponent alloys termed high-entropy alloys (HEAs).

HEAs are defined as multicomponent alloys containing 5 or more constituents in equiatomic or near equiatomic ratio [1]. They tend to exhibit solid solution structures, instead of complex phases, stabilized by their high configurational entropy of mixing. HEAs have shown some fascinating properties, like high strength [4], high fracture toughness at cryogenic temperatures [5], enhanced thermal stability [6], superior oxidation [7, 8], and corrosion resistance [9]. The advent of HEAs has also generated a lot of fundamental curiosities and led to the investigation of hitherto unexamined questions: atomic occupancy in a multicomponent lattice, visualization of higher dimensional phase diagrams, entropy contribution to phase stability, and atomic transport in multielement matrices being some of them. HEAs have been produced by melting and casting route, powder metallurgical synthesis, and deposition techniques [1]. While the bulk HEAs form the major share of HEAs synthesized so far, nanocrystalline HEAs have also been consistently developed. Nanocrystallinity adds another exciting facet to the vast compositional space and complex dimensions of HEAs. Nanostructured HEAs have shown improved mechanical properties [10], excellent magnetic behavior [11], and high thermal stability [12].

Mechanical alloying (MA) is a well-known solid-state, non-equilibrium, top-down approach to produce nanocrystalline materials. It involves milling of elemental powders to achieve alloying at atomic scale. MA process is described by the repeated welding and fracturing of powder particles entrapped between milling media, extent of which depends on the mechanical attributes of powder constituents [13]. Originally invented to produce oxide dispersion strengthened (ODS) alloys [14], the technique has been successfully applied to produce a variety of materials, like intermetallics, ordered compounds, solid solution alloys, amorphous structures, quasicrystalline phases, and nanocomposites [15]. In addition to nanoscale processing, MA also offers the advantage of extended solid solubility even in immiscible systems. It can be attributed

https://doi.org/10.1557/jmr.2019.37 Published online by Cambridge University Press

© Materials Research Society 2019

to the enhanced diffusion rates due to nanosize of powder components before alloying. Therefore, besides increased configurational entropy, MA lends enhanced stability to solid solution phases in HEAs. The effect of various milling parameters, like type of milling, ball-to-powder ratio, milling speed, and milling time, has been well documented [13] and can thus help in tailoring the microstructure and properties of HEAs. Unlike chemical routes and deposition techniques to synthesize nanomaterials, large-scale production of powder is feasible through MA using devices like planetary ball mill, attritor mills, and uni-ball mills. This has already proven useful to produce plasma sprayed HEA coatings [16] and would be apt when nanocrystalline HEAs are to be processed at industrial scale.

The first synthesis of HEAs by MA is credited to Varalakshmi et al. [17], who produced nanocrystalline AlCrCuFeTiZn alloy in 2008. Since then, MA has progressively been used to produce nanocrystalline HEAs, as depicted in increased number of journal publications on mechanically alloyed HEAs (Fig. 1). Although several review articles have appeared on HEAs (see, e.g., [18, 19, 20, 21, 22]), only two reviews have been published so far, which discuss the aspects of HEAs produced by MA [23, 24]. The present review attempts to provide a comprehensive and critical analysis of potentials and limitations of mechanically alloyed HEAs. The aspects of phase evolution during MA and subsequent thermal exposure, structural and functional properties obtained, and challenges faced during MA of HEAs form the core sections of the current report.

Synthesis methodologies

Mechanical alloying

MA of nanocrystalline HEAs has been carried out in high-energy ball mills. The majority of HEA synthesis by MA utilizes planetary ball mills; some of the other variants include SPEX mills [25] and shaker rod mills [26]. Grinding vials and balls of WC, hardened chrome steel, ZrO_2, and stainless steel have been frequently employed. Both dry and wet millings have been commonly used to synthesize HEAs by MA. The most common process control agent (PCAs) used is toluene, while some others include *n*-heptane [27], dodecane [28], ethanol [29], methanol [30], cyclohexane [31], and stearic acid [32]. Ar atmosphere has frequently been employed [33, 34, 35] when dry milling of HEAs is carried out to avoid oxidation of powders. A combination of dry and wet milling has also been increasingly used to produce HEA powders. To illustrate, $Al_{0.8}CoCrFeNiTi_{0.2}$ and $Al_{0.8}CoFeNiTi_{0.2}$ HEAs have been prepared by 45 h of dry milling, followed by 4 h milling in ethanol [36]. The effects of milling parameters, like milling speed, type of mills, milling time, milling media, and atmosphere of milling, have been fairly well understood for conventional alloys [15]. For HEAs, a systematic investigation for influence of these factors, barring milling time, is scarce in the literature. Salemi et al. [37] have shown that alloying is not complete in AlCoCuNiZn even after 50 h of milling when the balls of diameter 20 mm and rotation speed of 300 rpm are used. However, on increasing the milling speed to 350 rpm and using balls of varying diameter (20, 16, and 10 mm), single-phase FCC is obtained. The energy transferred to the powders is estimated to be 1.7 times higher in the latter case and hence accounts for the complete alloy formation. Tan et al. [38] synthesized $Al_2NbTi_3V_2Zr$ in low-energy (150 rpm) and high-energy (350 rpm) modes and showed that only high-energy mode is effective in alloying and achieving nanocrystallinity. CoCrFeMnNi shows a single-phase FCC structure when synthesized using WC vials and balls [39], while a minor BCC peak is observed when the alloy is milled in stainless steel media [40]. This can be attributed to the incorporation of excess Cr from stainless steel media during milling.

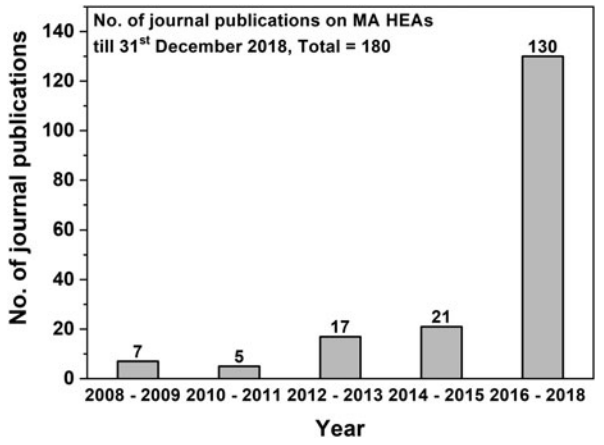


Figure 1: Number of journal publications on mechanically alloyed HEAs.

The influence of milling time on phase evolution is an obvious outcome of most of the reports on synthesis of HEAs by MA. The extent of alloying during milling is often determined by taking X-ray diffraction (XRD) patterns of powders at regular intervals. Most of the solid solution phases in HEAs form within 15–40 h of milling. Prolonged milling hours are often used for production of amorphous HEAs. AlBCFeNiSi and AlBCeFeNiSi alloys [41] show complete amorphization after 140 h of milling, while duration of 240 h is required to get amorphous phase in AlBFeNiSi [42]. While the extended milling time leads to more homogenous alloy formation, it also increases the likely contamination induced during milling. Therefore, sometimes, powders are milled only for short milling time and then annealed or consolidated to achieve the alloy formation. This is referred to as mechanical activation. Colombini et al. [43] used mechanical activation to synthesize AlCoCrFeNi, which involved ball milling for 1 h, followed by spark plasma sintering (SPS) at 1000 °C. The final alloy showed a mixture of BCC and FCC phases. MA for 35 h

https://doi.org/10.1557/jmr.2019.37 Published online by Cambridge University Press

© Materials Research Society 2019

followed by SPS at 1000 °C also led to the similar structure. Al_2O_3 dispersed AlCoCrFeMnNi alloys were synthesized by mechanical activation, followed by pyrolysis at 500 °C for 1 h [44]. A slightly modified approach has recently been reported by Kang et al. [45], where a minimum milling time is identified based on average HEA ($Al_{0.1}$CrMoNbV) powder size and interlamellar spacing. Although alloying is not complete at this milling time, it goes to completion during consolidation. In a very recent study [46], cryomilling of bulk cast ingots of AlCrFeMnV and CoCrFeMnNi has been performed to produce nanocrystalline HEAs. Large-scale production of powders and lower contamination serve as the major advantages of mechanical milling of HEAs.

One of the intuitive questions in the context of MA of HEAs is the role of configurational entropy on alloying kinetics. While the HEAs are expected to stabilize the solid solution structure, can they accelerate the rate of alloy formation during MA? Vaidya et al. [39] have shown in their recent report that the milling times required to obtain single-phase FCC in FeNi is 20 h, while for CoFeNi, CoCrFeNi, and CoCrFeMnNi, it is 15 h. Varalakshmi et al. [47] reported the synthesis of Al–Co–Cu–Ni–Ti–Zn system from binary CuNi to hexanary AlCoCuNiTiZn and 20 h of milling was required in each case for phase formation. This indicates that the increased configurational entropy does not have a significant effect on the dissolution rates during MA.

The conventional way to form HEA by MA requires mixing individual elements in required proportion in a single step. Phase formation, therefore, is governed by inherent thermodynamic and kinetic factors of the system. Vaidya et al. [48] have proposed a new approach to produce HEAs by MA, which involves step by step addition of constituent elements. This strategy is termed as sequential alloying and is schematically presented in Fig. 2(a). They have illustrated it through the formation of nanocrystalline AlCoCrFeNi by MA. For example, first, binary CoNi is formed by milling elemental Co and Ni powders. In the subsequent steps, Fe, Cr, and Al are added to form ternary (CoFeNi), quaternary (CoCrFeNi), and then quinary (AlCoCrFeNi) alloys, respectively. Similarly, AlCoCrFeNi was produced by 13 different sequences. The path dependence of phase formation was indicated in varied fractions of BCC and FCC phases obtained at the end of each sequence [Fig. 2(b)].

Consolidation techniques

Milled powders need to be consolidated to obtain dense pellets for measuring various mechanical and functional properties. The sintering method is usually chosen to achieve the best combination of density and nanocrystallinity. SPS has been the most widely used technique to consolidate milled HEA powders. The other sintering methods used typically include vacuum hot pressing sintering (VHPS) [35, 49, 50, 51, 52], microwave sintering [53], and hot isostatic pressing (HIP) [54]. Nearly instantaneous heating of powder particles occur due to the application of high-amperage pulsed current during SPS [55]. It implies that shorter times are required for consolidation during SPS relative to conventional sintering. Thus, the time available for grain growth is significantly less and better retention of nanocrystallinity is expected through SPS. To illustrate, AlCoCrCuFeTi$_x$ HEAs prepared by MA exhibit grain sizes of the order of 13–20 nm, which increase to 45–50 nm during SPS at 1173 K [56]. Nanocrystallinity is retained in Al–Co–Cr–Cu–Fe and Co–Cr–Cu–Fe–Ni milled powders consolidated using SPS [57].

However, in many cases, it has been observed that SPS is not able to retain the crystallite size strictly in the regime

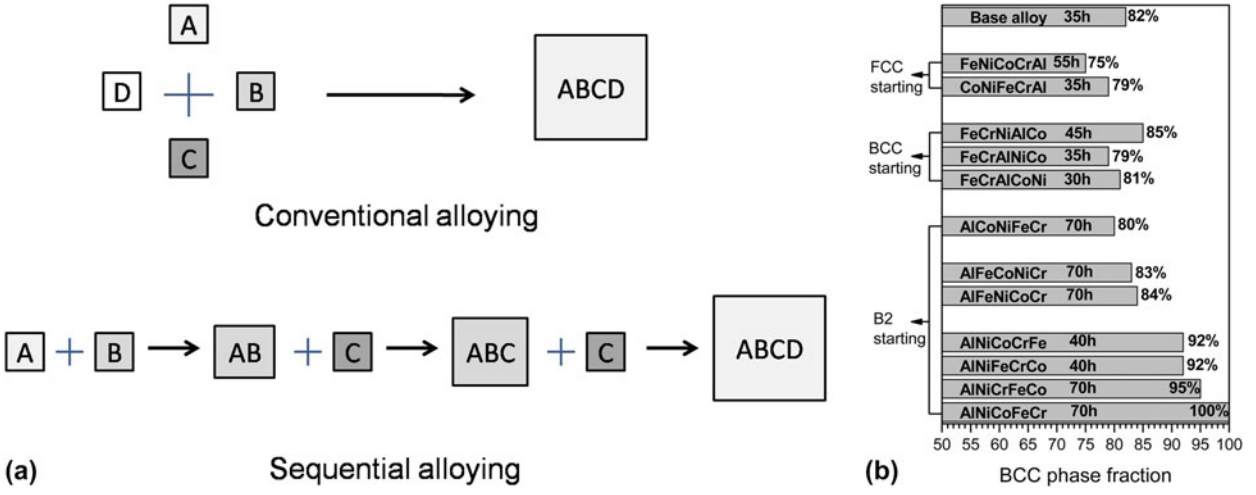


Figure 2: (a) Scheme of conventional alloying versus sequential alloying. (b) Phase fractions of BCC phase obtained in AlCoCrFeNi synthesized through different sequences [48].

https://doi.org/10.1557/jmr.2019.37 Published online by Cambridge University Press

© Materials Research Society 2019

(<100 nm) of nanocrystalline HEAs. Joo et al. [58] reported that the average grain size of CoCrFeMnNi HEA obtained after 60 h of MA is 11 nm. SPS at 1173 and 1373 K lead to increase in grain size up to 0.28 μm and 1.87 μm, respectively. Wang et al. [59] have demonstrated that for $CoCr_{2-x}CuFeNi_x$ HEAs, grain size grows from 10 nm to several hundred nanometers during SPS. Thus, the grain growth rates during SPS are relatively high, which corroborate with the recent results on non-sluggish grain boundary diffusion in HEAs [60]. An optimum combination of various SPS parameters is often needed to achieve desired densification and avoid coarsening of nanocrystallites. SPS of CoCrFeNi HEA powders at 800 °C resulted in a relative density (ρ_{rel}) of 0.84 and a crystallite size (d) of 35 nm. When SPS of same powders was carried out at 900 °C and 1000 °C, (ρ_{rel}, d) values are (0.95, 60 nm) and (0.95, 80 nm), respectively, which clearly indicate the optimum temperature of sintering to be 900 °C [61]. Recent studies on SPS have shown that applying a maximum pressure at higher temperature helps in better bonding between the powder particles and enhanced ductility [62].

The densification mechanisms of HEAs during sintering have not been probed extensively so far. SPS for most of the HEAs is carried out at temperatures well below melting point and hence densification proceeds mostly by solid-state sintering. Mane et al. [63, 64, 65] have attempted to understand the sintering mechanism of mechanically alloyed (MAed) and annealed CoCrFeNi and CoCrFeMnNi. Sintering of annealed powders is controlled by volume diffusion, while complex combination of ultrafine grains, high grain boundary fractions and chemical homogeneity governs the densification of milled powders. Mane and Panigrahi [66] have demonstrated that the increasing configurational entropy from CoFeNi to AlCoCrFeMnNi leads to reduced densification rates owing to increased activation energies of diffusion with increasing number of elements. Varalakshmi et al. [54] have shown that better densification rates in AlCrCuFeTiZn are achieved with HIP, compared with conventional sintering and VHPS. The evolution of phases also has been shown to differ if the consolidation technique is varied [52]. SPS has also been used to facilitate reactive sintering of SiC and AlCoCrFeNi HEA to produce composites with isomorphic structures and improved mechanical properties [67]. AlCoCrFeNi HEA consolidated using microwave sintering exhibited larger fraction of porosity than SPS and this difference is reflected in their respective mechanical properties [43].

Phase evolution during MA and consolidation

Solid solution formation rules

HEAs have tendency to show solid solution phases, which is attributed to their enhanced configurational entropy of mixing (ΔS_{config}). High ΔS_{config} reduces the free energy (ΔG_{mix}) of solid solution formation in accordance with the equation $\Delta G_{mix} = \Delta H_{mix} - T\Delta S_{mix}$, where ΔH_{mix} is the enthalpy of mixing and ΔS_{mix} is the entropy of mixing. ΔS_{mix} is summation of two entropy contributions, namely, thermal and configurational. Following Boltzmann analysis, the expression for ΔS_{config} is given as $\Delta S_{config} = -R\sum X_i \ln X_i$, where X_i is mole fraction of ith constituent and R is universal gas constant. This attains maximum for equiatomic composition, for which, $X_i = 1/n$ and hence $\Delta S_{config\ (max)} = R \ln n$ (n is the number of elements in the alloy). As an increasing number of HEAs are studied, it has been observed that the configurational entropy is not alone sufficient to stabilize the solid solution [22]. Consequently, a number of thermodynamic and topological parameters have been put forward to determine the criteria for solid solution formation [68]. For instance, Zhang et al. [69] argued that following conditions need to be satisfied for solid solution formation.

$$\Delta S_{config} > 1.61R,\ -15\ \text{kJ/mol} < \Delta H_{mix} < 5\ \text{kJ/mol and}\ \delta < 6.6\%\quad,$$

where δ is the size factor, $\delta = \sqrt{\sum C_i(1 - r_i/\text{avg} \cdot r_i)^2}$, and r_i is the atomic size of ith element. Guo et al. [70] showed that valence electron concentration (VEC) will play a major role in deciding the type of solid solution as follows—VEC ≤ 6.87: BCC solid solution, VEC ≥ 8: FCC solid solution, and 6.87 ≤ VEC ≥ 8: FCC + BCC. These rules can be used to predict the major phase formed after MA and consolidation.

To illustrate, Kumar et al. [71] explained the formation of FCC and BCC phases in $AlCoCrCuFeNiSi_x$ HEAs on the basis of VEC, Ω, δ, and mismatch entropy. However, in many cases, the parametric approaches can only predict the major phases formed during MA and sintering. For example, CoCrFeMnNi HEA formed by casting and MA displays a single-phase FCC structure [1], which is in accordance with the Ω, δ, and VEC parameters. However, SPS of MAed CoCrFeMnNi powders leads to the formation of Cr_7C_3. During MA at room temperature, the FCC structure is supersaturated with Cr, which diffuses out of lattice and forms carbide when exposed to high temperatures during SPS [39]. Similar instance of precipitation of ordered phase in CoCrCuFeNi [57] and σ phase in AlCoCrFeNi [72] could not be predicted using the above parameters. Some exceptions to these rules have also been observed. Dwivedi et al. [32] observed a single-phase FCC structure in CrNbTiVZn HEA, which has VEC of 6.4 and hence predicted to have a BCC structure.

HEAs with simple solid solution phases

The maximized configurational entropy of HEAs is expected to result in simple solid solution structures. Furthermore, MA

https://doi.org/10.1557/jmr.2019.37 Published online by Cambridge University Press

© Materials Research Society 2019

TABLE I: Single-phase HEAs observed during MA and consolidation.

Alloy	Phase	Consolidation technique	Phases (major + minor)	Ref.
CoCrFeMoNi	FCC	SPS	FCC	[73]
AlCoCrFeNi	BCC	...	...	[33, 74, 75]
$CoCrFeMnNiN_x$	FCC	VHPS	FCC + σ + $Cr_{23}C_6$ (x = 0) FCC + σ + $Cr_{23}C_6$ + Cr_2N (x = 0.1)	[49]
$Co_{25}Cr_{21}Fe_{18}Mo_8Nb_3Ni_{23}WC_2$	FCC	HPS	FCC + M_6C	[26]
AlCoCrFeMnNi	BCC	Microwave sintering	BCC + $L1_2$	[76]
AlCoCrFe	BCC	SPS	B_2 + $Cr_{23}C_6$	[62, 77]
$Al_{0.3}$CoCrFeMnNi	FCC	SPS	FCC + B_2 + Cr carbide	[78]
$AlCoCrCuFeNiTi_x$	BCC (x = 1, 2)	SPS	BCC	[56]
MoNbTaVW	BCC	SPS	BCC + Ta_2VO_6	[34]
$Al_{0.8}CoFeNiTi_{0.2}$	BCC + FCC	SPS	BCC + FCC	[36]
$Al_{0.8}CoCrFeNiTi_{0.2}$	BCC + FCC	SPS	FCC + BCC	[36]
AlCoCrFeNi	BCC	SPS	FCC + BCC	[43]
CoCrFeMnNi	FCC	VHPS	FCC + M_7C_3 + $M_{23}C_6$	[50]
AlFeTi	BCC	...	...	[17]
AlCrFeTi	BCC	...	...	[17]
AlCrFeTiZn	BCC	...	...	[17]
AlCrCuFeTiZn	BCC	CS	BCC	[17]
AlCoCuNiTiZn	BCC	...	...	[17]
CrCoFeMnNiW	BCC	...	...	[17]
CoFeNi	FCC	SPS	FCC	[57]
CoCuFeNi	FCC	SPS	FCC1 + FCC2	[57]
$Al_{0.5}CoFeNiTi_{0.5}$	FCC	SPS	FCC + BCC	[29]
$Al_{0.6}CoNiFeTi_{0.4}$	FCC	VHPS	BCC1 + BCC2 + FCC	[52]
BCoCrFeNi	FCC	...	...	[79]
BCrFeNiTi	BCC	...	...	[79]
BCrFeNiZr	BCC	...	...	[79]
$Al_{7.5}Co_{25}Cu_{17.5}Fe_{25}Ni_{25}$	FCC	SPS	FCC	[80]
AlCoCrFeNiTi	BCC	...	...	[81, 82]
$AlCoCrFeNiTi_{0.5}$	BCC	SPS	B_2 + FCC + σ + TiC	[30]
CoCrFeMnNi	FCC	SPS	FCC	[83, 84]
$AlCrCoCuFeZn_x$	FCC (x = 1, 1.5, 2)	...	...	[85]
AlCoCuNiZn	FCC	SPS (600–900 °C)	FCC1 + FCC2	[86]
AlCoCuNiZn	FCC	...	...	[37]
AlCrCuFeNi	BCC	PS	BCC + FCC1 + FCC2	[87]
AlCuFeNiTi	BCC	PS	BCC + FCC1 + FCC2	[87]
CrNbTiVZn	FCC	...	...	[32]
$Al_{0.3}$CoCrFeMnNi	FCC	SPS	FCC + B_2 + Cr carbide	[78]
AlCoCrFe	BCC	SPS CS	BCC/B_2 + $Cr_{23}C_6$	[77]
AlCrCuFeTiZn	BCC	VHPS HIP	BCC + FCC	[54]
$Co_xCrCuFeMnNi$	FCC (for x = 1, 1.5, 2)	...	...	[88]
MoNbTaW	BCC	...	...	[89]
$AlCoCrFeNiSi_x$	BCC (x = 0.3, 0.6, 0.9)	SPS	BCC + FCC + σ	[90]
CoCrFeMnNi	FCC	Hot pressing	FCC + M_7C_3	[91]
NbTaTiV	...	SPS	BCC	[92]
$Al_{0.1}$CrNbVMo	BCC	SPS	BCC	[45]
WMoNbZrV	BCC	...	...	[93]
AlCoCrFeNi	BCC	...	...	[94]

has been shown to extend solid solubility even in immiscible systems like Fe–Cu [13]. Therefore, the propensity of getting simple solid solution phases is higher during MA of HEAs. Table I lists the various HEAs, which show single-phase structure when processed by MA. Both single-phase FCC and BCC HEAs have been produced by MA, while no hexagonal close pack (HCP) system has been obtained by milling so far. CoCrFeMoNi shows a single-phase FCC structure [73], while AlCoCrFeMnNi crystallizes in BCC structure [76]. Non-equiatomic HEAs, like $Al_{0.3}$CoCrFeMnNi, have also shown single-phase structure during MA [78]. $AlCoCrCuFeZn_x$ [85] and $AlCoCrCuFeNiTi_x$ [56] exhibit FCC and BCC structures, respectively. Light HEAs (density <3 g/cm^3) is a class of HEAs being developed to achieve high specific strength suitable for energy-saving applications. These alloys contain elements like Mg, Li, and Be, and hence, it is challenging to produce them by liquid metal route. MA, if performed in an inert atmosphere, could prove useful to produce light HEAs. Youssef

https://doi.org/10.1557/jmr.2019.37 Published online by Cambridge University Press

© Materials Research Society 2019

et al. [95] processed single-phase FCC structured AlLiMgScTi HEA by MA.

HEAs with multiple solid solution phases are commonly observed, particularly in the non-equiatomic systems, as is evident in Table II. The formation of multiple phases in multielement HEAs is primarily governed by the thermodynamic interaction between binary constituents. To illustrate, in Al–Co–Cr–Fe–Ni system, B_2 phase observed is rich in Al–Ni, BCC phase is rich in Cr–Fe, and FCC phase is enriched in Co–Fe–Ni [110], which correlates with the phases observed in their respective binary phase diagrams [129]. Praveen et al. [57] highlighted the role of enthalpy in evolution of phases during MA and SPS and showed that complex σ phase precipitates in AlCoCrCuFe and CoCrCuFeNi. The phase evolution during MA and consolidation is often different from that observed during casting. While the high melting phase usually forms first during liquid metal processing routes, kinetics of dissolution during MA is further determined by factors like room temperature diffusivity, atomic radius, and ease of nanocrystallization. AlCoFeMoNiTi exhibits BCC solid solutions in the sintered and as-cast state, with additional CoMo-rich phases present in sintered condition. Fine alumina particles are also seen in sintered sample [114]. Cu separates out as an FCC phase during casting of HEAs like CoCuFeNi, while a single-phase FCC structure is observed when it is made by MA (Table I). A single-phase FCC structure is seen for as-cast CoCrFeMnNi, whereas mixture of FCC and Cr_7C_3 is observed when the HEA is processed by MA + SPS [39, 130]. Chen et al. [131] demonstrated that the alloying rate varies in the order Al → Co → Cr → Cu → Fe → Mo → Ni → Ti, which correlates with the melting point of the elements and consequently their room temperature diffusivities. It may be noted that the complex phases are formed, excluding the trace contaminations from milling media, which have not been observed during MA of HEAs.

The simple solid solution structures formed during MA are often metastable in nature and undergo phase transitions to different solid solution and complex phases on consolidation (Tables I and II). To illustrate, a mixture of FCC and BCC phases in AlCoCuNiTiZn is retained on annealing at 800 °C, while VHPS at the same temperature results in the formation of two FCC phases and a BCC phase [51]. $CoCrFeMnN_{0.1}Ni$ shows a single-phase FCC structure after 45 h of MA, while VHPS of the milled powders gives σ, $Cr_{23}C_6$, and Cr_2N phases [49]. AlCrCuFeMnW exhibits FCC and BCC phases after MA, which transforms to a mixture of BCC + AlFe type + FeMn type + σ (Cr-rich) phases [99]. SPS of BCC-structured NbMoTaVW leads to the formation of Ta_2VO_6 phase [34]. $Al_{0.5}CoFeNiTi_{0.5}$ undergoes phase transition from FCC to FCC + BCC during SPS [29], while FCC phase in $Al_{0.6}CoFeNiTi_{0.4}$ transforms to two BCC phases and an FCC phase during VHPS [52]. Growth of Cr-rich σ phase occurs in Cu_2Mg phase of $AlCrCuFeMg_x$ HEAs owing to the positive enthalpy of mixing between binary constituents [121]. A decomposed microstructure (FCC + $L1_2$ + σ) of AlCoCrFeMnNi HEA obtained after MA + SPS shows high hardness and better densification but suffers from poor fracture toughness [72].

Amorphous HEAs

Since the advent of HEAs, glasses or amorphous alloys with high configurational entropy have been explored. Cantor et al. [2] studied glass formation in (Ti, Zr, Nb, Hf)–(Ni, Cu, Ag)–Al system, which was formed by equiatomic substitution in Zr–Cu–Al glass-forming alloy. Ma et al. [132] reported the first equiatomic bulk metallic glass (BMG) in CuHfNiTiZr in the form of a 1.5 mm rod through Cu mold casting. Ge et al. [133] reported amorphous phase formation in AlCuNiTiZr HEAs based on $Cu_{60}Zr_{40}$ binary glass composition. These alloys can be referred to as pseudo-binary alloys, which are formed by suitable substitution in binary or ternary glass forming alloys. Some other pseudo-binary alloys reported include AlBFeNiSi [42] and BeCoMgTi and BeCoMgTiZn [134], which can be thought to be based on $Fe_{80}B_{20}$ and $Ti_{80}Be_{20}$ glassy compositions, respectively. The alloys such as AlCoCr-$Cu_{0.5}$Ni [131, 135, 136] and CrFeNbNiSi [79] have also been shown to exhibit amorphization during milling. These alloys do not fit under the category of pseudo-binary alloys but can be better referred to as true high-entropy glasses.

Prolonged milling hours have shown to produce amorphous phases in HEAs [131]. Al–Co–Cr–Cu–Fe–Mo–Ni–Ti alloys form solid solution phases and then change to amorphous structure on extended milling [135, 136], which conforms to first type of amorphization classified by Weeber and Bakker [137]. Amorphous phase is formed in BeCoMgTi and BeCoMgTiZn [134] by type II mechanism, as classified by Weeber and Bakker [137]. These alloys are particularly interesting as all the constituents have HCP structure, yet no solid solution structure is formed during milling. Vaidya et al. [79] studied the amorphization in CrFeNi–MX (M = Co, Mn, Nb, Ti, Zr metal and X = B, Si) alloys by MA. Although $Fe_{80}B_{20}$ is a good glass former, B containing HEAs did not form amorphous phase, except for M = Co. On the other hand, when B was replaced by Si, amorphous phase was observed for all M. Figure 3 shows the transmission electron microscope (TEM) micrographs illustrating the major amorphous phase formed in CrFeNi–ZrSi and the presence of nanocrystalline BCC structure in CrFeNi–ZrB. The lower melting point of Si and its larger size difference with other constituents enhance the amorphization in HEAs during MA. As presented in Table III, while many of the HEAs can be milled to fully amorphous structure, some alloys exhibit a minor amount of nanocrystalline solid solutions or undissolved elements.

https://doi.org/10.1557/jmr.2019.37 Published online by Cambridge University Press

© Materials Research Society 2019

TABLE II: MAed HEAs with multiple solid solution phases.

Alloy	Phases (major + minor)	Consolidation technique	Phases (major + minor)	Ref.
$CoCrCuFeMo_xNi$	FCC1 + FCC2 (for x = 0, 0.2)	SPS	FCC1 + FCC2 (for x = 0, 0.2)	[96]
AlCoCrFeNiSi	BCC + FCC	...	...	[97]
$AlCoCrCuFeNiTi_{0.5}$	BCC + FCC	SPS	BCC + FCC	[56]
MoNbTaWVTi	BCC1 + BCC2	SPS	BCC1 + BCC2 + FCC + TiO	[98]
AlCrCuFeMnW	BCC + FCC	SPS	BCC + AlFe type + FeMn type + σ (Cr-rich)	[99]
$CoCrFeMnNiC_{0.3}Ti_{0.3}$	FCC + BCC	VHPS	FCC + TiC + M_7C_3 + $M_{23}C_6$	[50]
AlCoCuNiTiZn	BCC + FCC	VHPS, HIP	BCC + FCC1 + FCC2	[47, 51]
CoCuNi	FCC1 + FCC2	...	...	[47]
CoCuNiZn	FCC1 + FCC2	...	...	[47]
AlCoCuNiZn	FCC1 + FCC2	...	...	[47]
AlCoCuNiTiZn	BCC1 + FCC1 BCC + FCC (x = 0, 8.33)	...	...	[47]
$AlCoCu_xNiTiZn$	BCC + FCC1 + FCC2 + FCC3 (x = 33) FCC1 + FCC2 + FCC3 (x = 49.98)	...	...	[47]
AlCoCrFeNiTi	BCC + FCC	SPS	B_2 + BCC + FCC	[100]
CoCrFeNi	FCC + BCC	SPS	FCC + σ	[57, 61, 101]
CoCrFeNi	FCC + BCC	SPS	FCC + Cr_7C_3 + Cr_2O_3	[12]
CoCrFeNi	FCC + BCC + σ	SPS	FCC + σ	[64]
CoCrCuFeNi	FCC + BCC	SPS	FCC1 + FCC2 + σ	[57, 61]
AlCoCrCuFe	BCC + FCC	SPS	B_2 + FCC + σ	[57]
$AlCoCrCuFe_xMo_{0.2}Ni$	BCC + FCC	...	...	[102]
$Al_{0.6}CoCrFeNiTi_{0.4}$	FCC + BCC	SPS	FCC1 + FCC2 + BCC	[103]
$Co_{0.5}CrFeNiTi_{0.5}$	FCC + BCC	SPS	FCC + σ	[104]
AlCrCuFeMnW	FCC + BCC	...	...	[105]
AlCrCuFeNiZn	BCC + FCC	HP	FCC1 + FCC2 + BCC	[106]
$Cr_{20}Cu_xFe_{20}Ti_{20}Zn_y$	FCC + BCC	SPS	FCC + BCC	[107]
CoCrCuNi	FCC + BCC	SPS	FCC1 + FCC2 + σ	[61]
CoCuFeNi	FCC + BCC	SPS	FCC1 + FCC2 + σ	[61]
AlCoCrCuFeNi	FCC + BCC	...	...	[108]
AlCoCrCuFeNiW	FCC + BCC	...	...	[108]
AlCoCrCuFeNiWZr	FCC + BCC	...	...	[108]
CoCrFeMnNi	FCC + BCC	...	...	[16]
CoCrFeMnNi	FCC + BCC	SPS	FCC	[40, 109]
AlCoCrFeNi	BCC + FCC	...	...	[16]
$Al_{0.5}C_{0.2}Co_{0.3}CrFeNi$	BCC + FCC	SPS	FCC + BCC + $Cr_{23}C_6$ + B_2	[110]
$CoCrFeMo_xNi$	FCC + BCC (x = 0.04) FCC + BCC + Mo (x = 0.2)	SPS	FCC + σ + μ	[101]
$CoCrFeNb_{0.08}Ni$	FCC + BCC	SPS	FCC + σ + NbC	[101]
$CoCrFeMo_{0.14}Nb_{0.14}Ni$	FCC + BCC + Mo	SPS	FCC + σ + μ NbC	[101]
AlCoCrFeMnNi	BCC + FCC	SPS	FCC + BCC	[111]
$Al_{0.6}CrFeNi$	BCC + FCC	SPS	FCC + BCC	[112]
$Al_{0.6}CoCrFeNi$	BCC + FCC	SPS, HP	FCC + BCC	[112]
$Al_{0.75}CrFeNi$	BCC + FCC	SPS	BCC + FCC	[113]
$Al_{0.75}CoCrFeNi$	BCC + FCC	SPS	FCC + BCC	[113]
$Al_{0.75}CoCrFeNiTi_{0.25}$	BCC + FCC	SPS	FCC + BCC	[113]
BCrFeMnNi	FCC + BCC	...	...	[79]
AlCoFeMoNiTi	BCC1 + BCC2	CS	BCC1 + BCC2 + CoMo-type phases	[114]
$Al_{0.5}CoCrFeNiTi_{0.5}$	FCC + BCC	SPS	FCC1 + FCC2	[29]
AlCoFeNiTi	BCC + FCC	SPS	FCC + BCC + Al_3Ti	[115]
AlCoFeNi(Cr, Cu, Mo, Ti)	BCC + FCC	...	...	[25]
$AlCrCuFeMgNi_{4.75}$	FCC + BCC	CS	Ordered FCC	[116]
$Co_{1.5}CrFeNi_{1.5}Ti_{0.5}$	FCC1 + FCC2 + BCC	SPS	FCC	[117]
$AlCoCrCuFeZn_{0.5}$	FCC + BCC	...	...	[85]
$CoCr_{2-x}CuFeNi_x$	FCC + BCC	SPS	FCC1 + FCC2 + σ	[59]
AlCrCuFeMnW	BCC + FCC	SPS	BCC + σ + AlFe type + FeMn type	[99]
AlCoCrFeNi	BCC + FCC	SPS, MWS	FCC + BCC	[43]
CoCrFeMnNi	FCC + BCC	HPS	FCC	[118]
CoCrCuFeNi	FCC + BCC	HPS	FCC	[118]
AlCoCrFeNi	BCC + FCC	SPS	FCC1 + $L1_2$ + σ	[72]
$CoCr_{0.25}CuFeNi_{1.5}V_{0.25}$	FCC + BCC	SPS	FCC1 + FCC2 + $(V, Cr)_7C_3$	[119]
$Ni_{1.5}CoCuFeV_{0.5}$	FCC + BCC	SPS	FCC1 + FCC2 + V_2C	[119]
$CoCrFeMo_xNiW_{1-x}$	BCC + FCC	VHPS	FCC1 + FCC2 + NiW + CoCr	[120]

(continued)

https://doi.org/10.1557/jmr.2019.37 Published online by Cambridge University Press

© Materials Research Society 2019

TABLE II: MAed HEAs with multiple solid solution phases. (*continued*)

$AlFeCuCrMg_x$	BCC + FCC (x = 0 and 0.5) BCC1 + BCC2 (x = 1 and 1.7)	SPS	BCC1 + BCC2 (x = 0) BCC + ordered phase + Cu_2Mg (x = 0.5, 1, 1.7)	[121, 122]
$Al_{0.6}CoFeNi$	FCC + BCC	SPS VHPS	FCC + BCC BCC + FCC	[52]
$Co_{0.5}CrCuFeMnNi$	FCC + BCC	...	...	[88]
$Al_{0.4}CoFeNiSi_x$	FCC + BCC + Si (x = 0.1–0.5)	...	...	[123]
$Ni_{1.5}Co_{1.5}CrFeTi_{0.5}$	FCC + HCP + Ni_3Ti + Tio	SPS	FCC + Ni_3Ti + TiO	[124]
CoFeMnNiV	FCC + BCC + σ	...	...	[125]
$Al_xCoCrFeMnNi$	FCC + BCC (x = 0.1–1)	Hot pressing	FCC + BCC + Al_2O_3 + M_7C_3 + $M_{23}C_6$	[91]
$Al_{0.15}CoCrCuFeNiTi_x$–C (x = 0, 1, 2)	BCC + FCC	SPS	FCC + BCC + $Cr_{23}C_6$ + TiC + σ	[126]
CuCrFeTiZn	BCC + FCC	SPS	FCC + BCC + $Ti_{2.84}Zn_{22.13}$ + FeTi	[127]
$CuCrFeTiZnPb_x$	Pb + BCC + FCC (x = 0.05, 0.1, 0.2)	SPS	FCC + BCC + $Ti_{2.84}Zn_{22.13}$ + FeTi + Pb	
$FeCoNiSi_{0.4}Al_{0.4}$	FCC + BCC	...	...	[128]

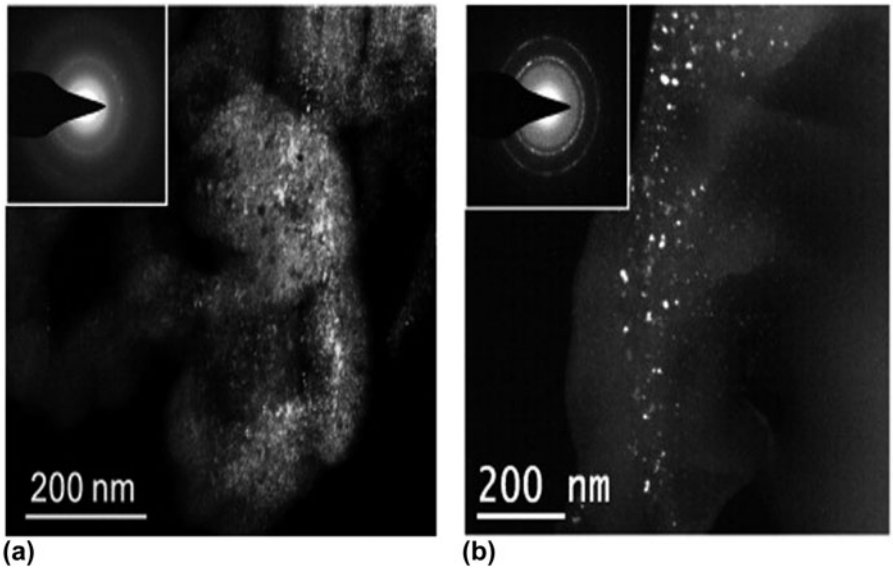


Figure 3: Dark-field image and corresponding selected area diffraction (SAED) patterns (shown in inset) depicting presence of (a) amorphous phase in FeCrNi–ZrSi and (b) nanocrystalline BCC structure in FeCrNi–ZrB [79].

Co addition has been to shown to enhance the glass-forming ability of AlBFeNiSi alloys, indicated in shorter time to get amorphous structure and higher onset temperature of crystallization [138, 143]. A similar effect of shortening the time to amorphization has been observed on C and Ce addition to AlBFeNiSi HEA [144] and Ti addition to AlCuZr [145]. C and Ce both enhance the thermal stability of amorphous phase in AlBFeNiSi alloy [144]. Cu and Ag, on the other hand, have detrimental effect on thermal stability of amorphous phase in AlBFeNiSi alloy. Higher amount of ductile elements, like Cu and Ni, increases the thermal stability of amorphous phases in $Al_{10}(CuNi)_{90-x}Ti_x$ alloys. The amorphous phases formed in (Ti, Zr–Nb)–(Cu, Ni)–Al system exhibit a large supercooled region (~125 K), indicating a high thermal stability again crystallization [139]. Annealing of amorphous HEAs can lead to the formation of simple solid solution phases or complex phases. AlBCoFeNiSi and AgAlBFeNiSi show greater phase stability than AlBFeNiSi and AlBCuFeNiSi HEAs, as indicated by the appearance of simple solid solution structures and complex phases, respectively, on annealing [146].

Effect of alloying elements

Several investigations have been performed to understand the influence of various elements during MA of HEAs. Atomic radius, crystal structure, and enthalpy of mixing with other constituents are the key criteria, which determine the elemental effect on phase formation. Al has the most significant effect on phase evolution in HEAs. It has FCC crystal structure but forms ordered BCC compounds with most of the common constituents like Co, Fe, and Ni. Therefore, most of the Al–Co–Cr–Fe–Ni systems show BCC as the major phase at higher Al

https://doi.org/10.1557/jmr.2019.37 Published online by Cambridge University Press

© Materials Research Society 2019

TABLE III: Amorphous HEAs formed by MA.

Alloy	Phases	Ref.
$AlBCo_xFeNiSi$	Amorphous	[138]
$Al_{10}(Ti_{0.33}Zr_{0.33}Nb_{0.33})_x(Cu_{0.5}Ni_{0.5})_{90-x}$	Amorphous + solid solution (x = 20–60) Solid solution + amorphous (x = 10, > 70)	[139]
$AlCoCrCu_{0.5}Ni$	Amorphous	[131, 135, 136]
$AlCoCrCu_{0.5}FeNi$	Amorphous	[131, 135, 136]
$AlCoCrCu_{0.5}FeNiTi$	Amorphous	[131, 135, 136]
$AlCoCrCu_{0.5}FeMoNiTi$	Amorphous	[131, 135, 136]
$Al_{10}(CuNi)_{90-x}Ti_x$	Amorphous	[140]
BeCoMgTi	Amorphous	[134]
BeCoMgTiZn	Amorphous	[134]
AlCoCrFeNiTi	Amorphous + BCC	[141]
AlBFeSiNbNi	Amorphous	[142]
AlBFeNiSi	Amorphous	[42]
CoCrFeNiSi	Amorphous + BCC	[79]
CrFeMnNiSi	Amorphous + BCC	[79]
BCrFeNbNi	Amorphous + BCC	[79]
CrFeNbNiSi	Amorphous + BCC	[79]
CrFeNiSiTi	Amorphous + BCC	[79]
CrFeNiSiZr	Amorphous + BCC	[79]
AlBCoFeNiSi	Amorphous	[143]
AlBCuFeNiSi	Amorphous	[143]
AgAlBFeNiSi	Amorphous + FCC	[143]
AlBCeFeNiSi	Amorphous	[144]
AlBCFeNiSi	Amorphous + Si	[144]
AlCuTiZr	Amorphous	[145]
AlCuNiTiZr	Amorphous	[35, 133]

content. Vaidya et al. [48] demonstrated the impact of Al in promoting BCC phase formation through sequential alloying. A single-phase BCC structure is obtained at the end of alloying sequence AlCoCrFeNi, while 75% of BCC phase is present for the sequence FeNiCoCrAl, where Al is added at the last step. Further, because of its high ductility, it causes relatively less erosion of milling media and therefore results in lower contamination levels. Al addition ($Al_{0.3}$CoCrFeMnNi) hardens and induces ordered B_2 precipitates in a soft FCC alloy based on CoCrFeMnNi [78]. Transition from single-phase FCC to FCC + BCC matrix has been demonstrated in sintered microstructure of Al_xCoCrFeMnNi HEAs for $x > 0.1$ [91]. Co, during MA, has been shown to undergo polymorphic transformation from HCP to FCC structure [141] and hence stabilizes FCC structure [48]. Co promotes FCC phase formation, and its removal from $Al_{0.75}$CoCrFeNi and $Al_{0.6}$CoCrFeNi results in decreased fraction of FCC phase [52, 112]. Cr addition promotes the formation of BCC phase during MA [48] and has been shown to reduce the nanoscale twin formation when dissolved in FCC phase [29]. Cr containing HEAs have invariably been shown to form carbides on annealing and consolidation of milled powders [61, 62] due to its highly negative free energy of formation [147].

Earlier studies had identified them as σ phases [61], but detailed microscopy later confirmed the presence of carbides. Praveen et al. [62] argued that the Cr delays the densification rates in HEAs although leading to maximum final densification in 3d transition HEAs. Cu has positive enthalpy of mixing with most of the 3d transition elements and hence often separates out as FCC phase [106, 107]. $AlCoCu_x$NiTiZn HEAs exhibit FCC phase for all the values of x [47]. Cu-rich FCC phase is observed in AlCoCrCuFe during MA and SPS [57]. Mg addition leads to an increase in fraction of BCC phase in $AlCrCuFeMg_x$ HEAs [122]. An optimum hardness was achieved for $x = 0.5$ for these alloys consolidated by SPS [121]. The thermal stability of alloys was reduced with increasing content of Mg, as the transformation of solid solution structure occurs at lower temperatures [121]. The addition of Mo leads to the appearance of complex σ and μ phases in $CoCrCuFeMo_x$Ni (for $x = 0.6, 0.8$) [96] and $CoCrFeMo_x$Ni ($x > 0.04$) alloys [101]. Annealing at higher temperature leads to dissolution of Mo in $CoCrFeMo_x$Ni alloys but leads to the formation of Mo-rich μ phase and carbides [101]. Sun et al. [26] demonstrated that addition of amorphous Cr(Mo) powders accelerates the dissolution of Mo into FCC phase to produce a single-phase structure. Nb dissolves in FCC matrix of CoCrFeNi during MA but results in the formation of NbC on consolidation or heat treatment at high temperature [101]. Nb addition to AlBFeNiSi leads to an increase in time required to achieve amorphization but imparts high thermal stability and heat resisting properties to the alloy [142]. The increase in Ni/Cr ratio promotes the formation of FCC phase and more homogenous microstructure in $CoCr_{2-x}CuFeNi_x$ HEAs due to FCC structure of Ni [59]. The increase in the amount of Si increases the mismatch entropy ($\Delta S\sigma/k$), which facilitates the BCC phase formation over FCC phase in $AlCoCrCuFeNiSi_x$ HEAs [71] and further leads to complex phase precipitation at $x = 0.9$ [90]. Incorporation of Si to CrFeNi (M = Co, Mn, Nb, Ti, Zr) HEAs enhances the ease of obtaining amorphization, in contrast to B [79]. Addition of Ti enhanced the formation of nanotwins slightly in $Al_{0.6}$CoFeNiTi and $Al_{0.6}$CoCrFeNi$Ti_{0.25}$ HEAs [29, 95]. When added to Al-containing HEAs, Ti promotes the formation of BCC structure [56]. The mixing of Ti and C with CoCrFeMnNi results in the formation of composite microstructure containing carbides [110, 126]. Incorporation of W to magnetic AlCoCuCrFeNi converts it to partially paramagnetic, which on further addition of Zr results in completely paramagnetic AlCoCrCuFeNiWZr HEA [108].

Thermal stability of MAed HEAs

To advance the exploration of HEAs for high temperature applications, their performance needs to be adjudged by creep behavior, microstructural stability, and mechanical properties

https://doi.org/10.1557/jmr.2019.37 Published online by Cambridge University Press

© Materials Research Society 2019

at elevated temperatures. It is particularly critical for nanostructured HEAs as they have additional driving forces for grain growth, enhanced kinetics due to reduced diffusion distances, and hence have high proclivity for reduction in mechanical properties with temperatures. However, systematic study of thermal stability of nanocrystalline HEAs has been limited in the available literature. There are two aspects of thermal stability that need to be looked at for MAed HEAs, namely, stability of the phases formed and the retention of nanocrystallinity. Table IV lists the various investigations of phase stability of HEAs reported so far. Nanocrystalline AlCoCrFe reveals excellent phase stability and consequently enhanced resistance to annealing-induced softening [77]. Figures 4(a) and 4(b) compare the phase evolution in Al_xCoCrCuFeNi after MA for 20 h and heat treatment using differential scanning calorimetry (DSC) till 1480 °C, respectively [150]. The BCC + FCC1 + FCC2 structure of the as-milled $Al_{0.45}$CoCrCuFeNi and AlCoCrCuFeNi transformed to FCC1 + FCC2 mixture. $Al_{2.5}$CoCrCuFeNi exhibited B_2 structure after MA and its thermal exposure in DSC resulted in the appearance of FCC phase. The highest thermal stability was observed for Al_5CoCrCuFeNi, which retained its single-phase B_2 structure (except for formation of minor oxides) after DSC. Shivam et al. [94] showed that disordered BCC phase in AlCoCrFeNi partially transforms to $L1_2$ phase on annealing at low temperatures and to $B_2 + L1_2 + \sigma$ phases on thermal exposure at high temperatures. Vaidya et al. [39] studied the phase stability of nanocrystalline FCC HEA powders and SPSed pellets. Formation of Cr_7C_3 occurs on heat treatment (800–1100 °C) of CoCrFeNi and CoCrFeMnNi MAed powders, while retaining the major FCC phase (depleted in Cr). SPSed as-milled powders exhibited dominant FCC phase and a small fraction of Cr_7C_3, which is retained on thermal exposure at 1373 K. AlCoCuNiTiZn exhibits high thermal stability, retaining solid solution structure and nanocrystallinity on heat treatment at 800 °C for 1 h [47, 51].

Koundinya et al. [106] used DSC traces to determine the activation energy for recrystallization (~85 kJ/mol) for AlCrCuFeNiZn. Cr-rich BCC phase is observed in Cr-containing HEAs at the end of milling, which dissolves during sintering or heat treatment at elevated temperatures [150]. An interesting distinction observed between many HEAs and conventional alloys is the nature of room temperature phase in relation to the high-temperature phase. Pure elements and conventional alloys possess close-packed structure at room temperature and a more open structure at higher temperatures. Classic example in this regard is Ti, which changes from HCP to BCC at elevated temperatures. Furthermore, in conventional alloys, a disordered structure becomes ordered at lower temperatures. However, some HEAs are found to show an opposite tendency [57, 148]. High strain due to lattice distortion exists in complex matrix of HEA. A closed packed structure will have higher strains. Thus, atoms tend to crystallize in a more open structure at room temperature, so that additional strain can be compensated. Thermal exposure relives the extra component of lattice strain and existence of close-packed structure becomes more viable [1]. As noted in Table IV, complex phases also precipitate during annealing of MA powders and sintered pellets. Precipitation of $L1_2$ and Mn_3Co_7 phases is observed on heat treatment of BCC-structured AlCoCrFeMnNi formed by MA [76]. Heat treatment of FCC-structured $Co_{20}Cr_{20}Fe_{20}Mn_{5}Ni_{20}Zn_{15}$ powders at 500 °C for 1 h leads to the formation of complex phases α-FeCo, β-NiZn, and $Cr_{23}C_6$ [28]. AlCoCrFeMnNi HEA produced by mechanochemical synthesis has shown thermal stability up to 500 °C, after which it undergoes diffusional transformation to complex phases [53].

High resistance to grain growth has been observed in CoCrFeNi during long-term heat treatment (600 h) at 900 °C [12]. Nanocrystallinity of milled powders is retained in Al–Co–Cr–Cu–Fe–Ni HEAs even after heat treatment at elevated temperatures [150, 151]. Praveen et al. [12] demonstrated the exceptional resistance to grain growth observed for CoCrFeNi on long-term heat treatment at 900 °C for 600 h. Presence of fine oxide and carbide particles together with slow rates of diffusion was believed to be responsible for high thermal stability of the alloy. The activation parameters for grain growth in SPSed CoCrFeNi and CoCrFeMnNi HEAs have been determined (private communications). The activation energy (Q) values are 175 and 241 kJ/mol for CoCrFeNi and CoCrFeMnNi, respectively, which is in close agreement with the Q_{GB} of Ni grain boundary diffusion in these HEAs [60]. This highlights the key role of grain boundaries in determining thermal stability of nanocrystalline HEAs.

Properties of MAed HEAs

Mechanical properties

HEAs produced by MA and subsequent consolidation often get benefits of multiple strengthening mechanisms. The cast HEAs primarily derive their strength from solid solution strengthening and to some extent from fine precipitation, e.g., as observed in case of B_2 + BCC structured AlCoCrFeNi. For HEAs produced by MA and subsequent consolidation, grain boundaries (due to nanocrystalline nature), precipitates, and nanoscale twins formed during consolidation provide enhanced contributions to strength. SPSed CoCrFeNi exhibits hardness of 570 HV [101], which is nearly 4 times the hardness value (150 HV) of the as-cast CoCrFeNi [153]. AlCoCrFeNi processed by MA + SPS exhibits compressive yield strength of 2.6 GPa [72], which is twice the strength levels achieved for the as-cast alloy [154]. Formation of nanoprecipitates during MA and SPS imparts higher strength

https://doi.org/10.1557/jmr.2019.37 Published online by Cambridge University Press

© Materials Research Society 2019

TABLE IV: Phase stability of HEAs formed by MA and subsequent consolidation.

Alloy system	Processing route	Phases (major + minor)	Heat treatment condition	Phases (major + minor)	Ref.
AlCoCrFeMnNi	MA (40 h)	BCC	<500 °C 575–800 °C	BCC BCC + $L1_2$ + Mn_3Co_7	[76]
AlCoCrFe	MA + SPS	B_2 + $Cr_{23}C_6$	900 °C, 600 h	B_2 + $Cr_{23}C_6$	[77]
AlCoCrFeNi	MA + SPS	FCC + BCC	1200 °C, 50 h	FCC	[43]
AlCoCrCuFeNi	MA	FCC + BCC	500–1000 °C, 1 h	FCC + BCC	[148, 149]
AlCoCuNiTiZn	MA	BCC + FCC	800 °C, 1 h	BCC + FCC1 + FCC2	[51]
AlCoCrFeNiTi	MA	BCC + FCC	500–1000 °C, 1 h	BCC + FCC (<700 °C) BCC + FCC1 + FCC2 (>700 °C)	[100]
$Al_{0.45}$CoCrCuFeNi	MA	BCC + FCC1 + FCC2	DSC (till 1480 °C)	FCC1 + FCC2	[150]
AlCoCrCuFeNi	MA	BCC + FCC1 + FCC2	DSC (till 1480 °C)	FCC1 + FCC2	[150]
$Al_{2.5}$CoCrCuFeNi	MA	B_2	DSC (till 1480 °C)	B_2 + FCC	[150]
Al_5CoCrCuFeNi	MA	B_2	DSC (till 1480 °C)	B_2	[150]
CoCrFeNi	MA	FCC + BCC	900 °C	FCC + σ	[101]
			600 °C	FCC + BCC + σ	[64]
CoCrFeNi	MA	FCC + BCC + σ	800 °C	FCC + σ	...
			1100 °C	FCC	...
$CoCrFeMo_{0.2}Ni$	MA	FCC + BCC + Mo	400–900 °C	FCC + Mo (<500 °C) FCC + σ + μ + Mo_3Ni_3C (500–800 °C) FCC + σ + μ (900 °C)	[101]
$CoCrFeMo_{0.2}Ni$	MA + SPS	FCC + σ + μ	500–900 °C	FCC + σ + μ	[101]
AlCoCrCuFeNi	MA + SPS	FCC1 + FCC2 + BCC	400–600 °C	FCC1 + FCC2 BCC + Mn_3Co_7 (500 °C)	[151]
AlCoCrFeMnNi	MA	BCC + FCC	500–1000 °C	BCC + FCC + Mn_3Co_7 (600–700 °C) FCC + BCC + Mn_3Co_7 (800–1000 °C)	[111]
$CoCrFeMn_{0.5}NiTi_{0.5}$	MA	BCC	700 °C, 1 h	FCC	[152]
CoCrFeNi	MA + SPS	FCC + BCC	900 °C, 600 h	FCC + Cr_7C_3 + Cr_2O_3	[12]
$AlCoCrFeNiTi_{0.5}$	MA + SPS	B_2 + FCC + σ + TiC	1100 and 1250 °C, 2 h	B_2 + FCC + σ + TiC	[30]
AlCoCrFeNiTi	MA	BCC	APS (atmospheric plasma spraying)	BCC + FCC + B_2	[81]
$Al_2NbTi_3V_2Zr$	MA	BCC	1200–1550 °C	BCC + α + β	[38]
AlCoCrFeNi	MA + sintering (SPS, MWS)	BCC + FCC	1000 °C	FCC	[43]
AlCoCrFeNi	MA	BCC	425 °C −800 °C	BCC + B_2 + $L1_2$ + σ	[94]
AlCoCrFeMnNi	MA	BCC + FCC	1000 °C	FCC + BCC + Mn_3Co_7	[44]
AlBCFeNiSi	MA	Amorphous + Si	800 °C	FCC + BCC + Fe_3Si	[41]
AlBCeFeNiSi	MA	Amorphous + Si	800 °C	FCC + Fe_3Si + $CeAlO_3$	[41]
$Co_{20}Cr_{20}Fe_{20}Mn_5Ni_{20}Zn_{15}$	MA	FCC	500 °C, 1 h	FCC + α-FeCo + β-NiZn + $Cr_{23}C_6$	[28]
CoFeNi	MA	FCC	800–1100 °C	FCC	[39]
CoCrFe(Mn)Ni	MA	FCC + WC	800–1100 °C	FCC + Cr_7C_3	[39]
CoFeNi	MA + SPS	FCC	800–1100 °C	FCC	[39]
CoCrFe(Mn)Ni	MA + SPS	FCC + Cr_7C_3	800–1100 °C	FCC + Cr_7C_3	[39]
$Co_{0.5}$CrCuFeMnNi	MA	FCC + BCC	700–900 °C	FCC1 + FCC2 + σ	[88]
CoCrCuFeMnNi	MA	FCC	700–900 °C	FCC1 + FCC2	[88]
$Co_{1.5}$CrCuFeMnNi	MA	FCC	700–900 °C	FCC1 + FCC2	[88]
Co_2CrCuFeMnNi	MA	FCC	700–900 °C	FCC1 + FCC2	[88]
$Al_{0.4}CoFeNiSi_x$ (x = 0.1–0.5)	MA	FCC + BCC + Si	300–600 °C	FCC + BCC + $CoFe_2O_4$	[123]
MoNbTaW	MA	BCC	1200 °C, 2 h	BCC	[89]

to AlCoFeMoNiTi HEA than reported for the cast alloy [114]. Refractory NbMoTaVW HEA processed by MA and SPS has shown to exhibit significantly high compressive yield strength (2612 MPa) and a plastic strain of 8.8% at room temperature. The same HEA processed by arc melting route shows a compressive yield strength of 1246 MPa and a plastic strain of 1.7% at room temperature [34]. Nonequiatomic $Co_{1.5}$CrFeNi$_{1.5}$Ti$_{0.5}$ HEA, produced by SPS, exhibited attractive combination of mechanical properties (bend strength = 2.6 GPa, tensile strength = 1.4 GPa, microhardness = 4.4 GPa, and 4% tensile elongation to fracture), which are superior to conventional as-cast HEAs.

The combination of various strengthening mechanisms has resulted in the development of HEAs with exciting properties. Figure 5 shows the various contributions to strengthening assessed for Al_xCoCrCuFeNi HEAs, produced by MA + SPS, with increasing Al content. The solid solution strengthening increases with higher Al content, while the grain size

https://doi.org/10.1557/jmr.2019.37 Published online by Cambridge University Press

© Materials Research Society 2019

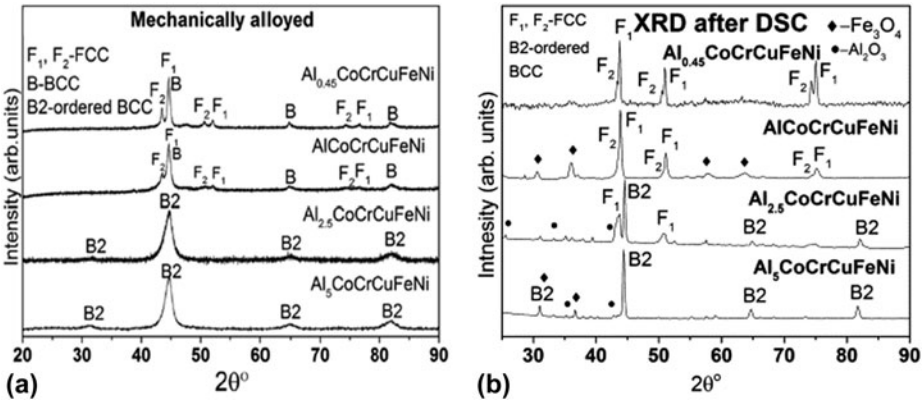


Figure 4: (a) Phase evolution of MAed $Al_xCoCrCuFeNi$ and (b) their thermal stability investigated using DSC till 1480 °C [150].

strengthening remains nearly same due to similar level of nanocrystallinity observed for all the alloys [151]. AlCoFeNiTi, after SPS, shows major FCC phase along with fine precipitates of B_2 phase and Al_3Ti particles [115]. Thus, solid solution strengthening, grain boundary strengthening, twin boundaries formed in FCC phase, and precipitation hardening, all contribute to give an ultra-high compressive strength of 2.9 GPa and a failure strain of 5.9% to the HEA [115]. Composite microstructure of FCC and M_6C carbides in $C_2Co_{25}Cr_{21}Fe_{18}Mo_8Nb_3Ni_{23}W$ exhibits attractive high temperature properties, namely, ultimate tensile strength of 795 MPa and elongation of 13.3% at 650 °C [26]. Presence of nano-sized TiO_2 particles and coherent Ni_3Ti precipitates in FCC matrix of $Co_{1.5}CrFeNi_{1.5}Ti_{0.5}$ imparts a good combination of strength (1460 MPa) and ductility (14.5%) [124]. $Al_{0.3}CoCrFeMnNi$ shows high compressive strength of 979 MPa and failure strains of 39%, resulting from the combination of ultrafine grained structure and presence of second phase formed during SPS [78]. The solid solution strengthening and nanocrystalline nature of AlCoCuNiTiZn impart a high compressive strength (>2.36 GPa) to the alloy, which is greater than most commercial hard-facing alloys [47, 51]. The nanocrystalline $Al_{7.5}Co_{25}Cu_{17.5}Fe_{25}Ni_{25}$ HEA exhibits an ultra-high compressive yield strength of 1795 MPa and a hardness of 454 HV. The calculated values of the quantitative contributions from solid-solution strengthening, twin boundary strengthening, dislocation strengthening, and grain boundary strengthening are 28, 71, 600, and 1136 MPa, respectively, suggesting that the ultra-high strength of the nanocrystalline $Al_{7.5}Co_{25}Cu_{17.5}Fe_{25}Ni_{25}$ HEA is primarily attributed to grain boundary strengthening and dislocation strengthening [80]. Hadraba et al. [83] showed that the increase in strength up to 30% at room temperature and 70% at elevated temperature could be observed for CoCrFeMnNi HEAs with nano Y_2O_3. The ODS alloy shows 3 times lower creep strain rates than the alloy without oxide particles, suggesting effective pinning mechanism.

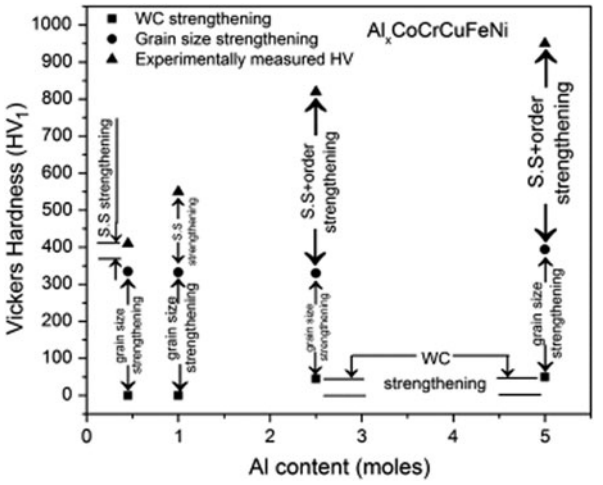


Figure 5: Various contributions to strengthening depicted for $Al_xCoCrCuFeNi$ HEAs as a function of Al content [151].

Chen et al. [113] demonstrated that the strength levels of Al–Cr–Fe–Ni alloys vary as $Al_{0.75}CrFeNi < Al_{0.75}CoCrFeNi < Al_{0.75}CoCrFeNiTi_{0.25}$ with Co and Ti addition, which is attributed to enhanced solid solution strengthening present in the HEAs. Light HEA AlLiMgScTi produced by MA shows a high hardness of 5.9 GPa because of its nanocrystalline structure [95]. Nanoscale twins formation has been observed in FCC phase formed during MA and SPS [29, 80, 95, 103, 106, 110, 119]. The presence of nanotwins along with the high solid solution strengthening results in excellent compressive properties of the alloy [103]. Age hardening during SPS of AlCoCuNiZn was demonstrated owing to fine precipitation of α phase within γ grains [86]. Threefold increase in hardness is observed during peak-ageing compared with as-milled and solutionized state [86]. Nonmetallic additions have also been made to HEAs to improve their mechanical properties. Addition of 0.1 at.% N to CoCrFeMnNi leads to increased ultimate compressive strength (by 154 MPa) and plasticity (by 9.9%) [49]. Solid solution strengthening, ultra-fine grain size,

https://doi.org/10.1557/jmr.2019.37 Published online by Cambridge University Press

© Materials Research Society 2019

interstitial strengthening (from C, O dissolved during MA and SPS), and presence of oxide inclusions contribute to the significant hardening achieved in the SPSed alloy [34]. AlCoCrFe shows excellent resistance to softening during annealing at 900 °C for 600 h, after which the drop in hardness is only 10% [77]. Exceptional retention of strength (~5 GPa) up to 600 °C has been demonstrated for nanocrystalline MoNbTaW HEA films [155]. They also have been shown to possess high strength to density ratio (>0.4 MJ/kg) and very low strain-rate sensitivity (~0.005), making them promising materials for high stress and high temperature applications [155].

Functional properties

The functional properties of HEAs have been studied relatively less than their mechanical behavior, yet some promising attributes have been observed for HEAs. Diverse and appealing properties like high hardness, reasonable ductility, and fracture toughness make HEAs suitable candidates for wear resistance applications. Varalakshmi et al. [54] demonstrated significantly reduced wear loss rates for AlCrCuFeTiZn HEA compared with commercially used Ni-hard faced alloy. The alloy was processed by MA, followed by HIP, and exhibited very high hardness of 10 GPa, which led to its excellent wear resistance. The wear behavior of CoCrFeMoNi has been observed to be superior to HFXP-58 [73]. The mechanical and tribological properties of the $(CuCrFeTiZn)_{100-x}Pb_x$ composites show a good combination of hardness (3.5–6 GPa), compressive strength, plasticity (15–20%), and wear resistance [127]. Atmospheric plasma sprayed AlCoCrFeNiTi coating showed good wear resistance at room temperature and at 500 °C, when compared with BCrNiSi alloy and stainless steel. Adhesive wear was identified as major wear mechanism at room temperature, while abrasive wear also takes place at higher temperatures [81]. AlCuNiTiZr HEA has been shown to possess better corrosion resistance than 304 stainless steel in the seawater environment as indicated by the higher corrosion potential, wider passivation region, and secondary passivation [35, 133]. $AlBCo_xFeNiSi$ exhibits semi-hard magnetism with a high value of M_s = 26.1 emu/g for x = 0.8 [138]. The soft magnetic properties of $Co_xCrCuFeMnNi$ (x = 0.5–2) alloys have been shown to improve with increasing cobalt content, with $Co_2CrCuFeMNNi$ exhibiting a high M_s value of 52 emu/g and coercivity of 14 Oe [88]. Ji et al. [40] demonstrated magnetic transition from soft magnetic to paramagnetic behavior when milled powders of CoCrFeMnNi HEA are consolidated using SPS. The saturation magnetization of AlBFeNiSi(Nb) HEAs decreases with increasing content of amorphous phase [142]. The addition of Co, Cu, Ce, and Ag has been shown to decrease the saturation magnetization of AlBFeNiSi alloys [143, 144], while C increases the saturation magnetization [144]. Annealed AlBFeNiSi(Co, Cu, Ag) alloys show improved magnetic properties due to the presence of FeB- and FeSi-rich phases [146]. Yang et al. [156] demonstrated that the crystalline $Al_{0.8}$CoCrFeNi exhibit superior electromagnetic wave absorption properties than its amorphous counterpart. CoCrCuFeNi exhibits higher M_s value than CoCrFeMnNi produced by identical processing route.

HEAs produced by HPT

Other than MA, high-pressure torsion (HPT) has increasingly been used to produce nanocrystalline HEAs. Therefore, it is worth comparing the salient features of HEAs produced by these two severe plastic deformation (SPD) routes. Like MA, HPT produces HEAs usually at room temperature and in few cases at cryogenic temperatures. Moon et al. [157] demonstrated that a diffusionless transformation from FCC to HCP structure occurs in $Co_{20}Cr_{26}Fe_{20}Mn_{20}Ni_{14}$ HEA during HPT at 77 K. The high strains imparted during HPT processing often result in the formation of metastable phases, which decompose during thermal treatment. AlNbTiV HEA formed by HPT exhibits a single-phase BCC structure. During annealing at temperatures above 700 °C, precipitation of Nb_2Al and Ti_3Al is observed [158]. It has been shown in the section "Amorphous HEAs" that prolonged milling times lead to the formation of amorphous HEAs. Similarly, use of very high strains during HPT generates excessive vacancies in the material, which result in appearance of new phases. To illustrate, at equivalent strain values, e = 50, HPT of HfNbTaTiZr forms a single-phase BCC structure, which decomposes into BCC and HCP phases at e > 100, as reflected in the loss of ductility and strength [159]. Wu et al. [160] demonstrated that continuous deformation during HPT of CoCrFeNi causes the nucleation and growth of amorphous phase at twin–twin intersected regions, owing to enhanced defect accumulation. Since alloying of elemental powders happens during milling, a wide range of HEAs can be produced by MA. HPT is performed often on a cast ingot and therefore deformation characteristics of the alloy determine its suitability for successful HPT processing. A novel methodology of using elemental powder mixture for HPT has been used by Kilmametov et al. [161] to produce nanocrystalline CoCrFeMnNi. Pressure of 5 GPa and shear strain equivalent to 100 rotations were used to drive the alloying during HPT. One distinct advantage of MA over HPT is the uniformity of microstructure obtained. For example, CoCrFeMnNi produced by MA and SPS showed a uniform microstructure of FCC and carbides, with a grain size of 185 nm. HPT processing of CoCrFeMnNi results in the formation of non-uniform microstructure, with grain sizes being 60 nm and 4 μm at periphery and center, respectively. The inhomogeneity

https://doi.org/10.1557/jmr.2019.37 Published online by Cambridge University Press

© Materials Research Society 2019

leads to the gradient in strength along the disc (5.3 GPa at periphery and 2.4 GPa at center). HPT is certainly a much cleaner process, with minimal risk of contamination that is frequently encountered in HEAs formed by MA. Also, consolidation of milled HEA powders is frequently performed, which leads to a slight increase in grain size. A much finer microstructure can be obtained using HPT. To illustrate, Shahmir et al. [162] obtained a grain size of ~10 nm in CoCrFeMnNi HEA, which exhibited superplastic elongations (>400%) at 873 and 973 K.

Together, MA and HPT form attractive options to produce a wide variety of nanocrystalline HEAs with exciting features and properties. Reports on processing of HEAs by other SPD routes, like equal angular channel pressing, have been scarce (see, e.g., Ref. 163), which certainly forms an area to be explored in future.

Potential applications

The field of HEAs can still be considered in early stages of development. Although 3d transition metal HEAs and refractory HEAs have shown some exciting features and properties, further enhancement in their processing and properties is required before they can compete with materials like superalloys [18]. One of the promising applications foreseen for HEA powders is in coatings. Cold spraying, plasma spraying, and thermal spraying are being used to produce HEA coatings. CoCrFeNi (Mo_xW_{1-x}) coatings exhibit good metallurgical bonding to Q235 steel substrate and possess superior strength and wear resistance than the substrate. Mo addition provides more protective coating as reflected in its more positive corrosive potential and reduced corrosion rates [120]. AlCoCrFeNiTi coatings produced by atmospheric plasma spraying show better strength and wear resistance than 316 stainless steel [81]. AlCoCrFeNiSi coating formed by atmospheric plasma spraying has shown good combination of mechanical and wear properties, making it suitable for abrasive environments [97]. Ang et al. [16] prepared AlCoCrFeNi and CoCrFeMnNi HEA coatings using thermal spraying. Both the coatings showed prominent FCC structure and consequently nearly same hardness (>4 GPa). The unique lamella structure is observed for AlCoCrFeNi coating and results in anisotropic mechanical response. Laser cladding of BCoCrFeNiSi self-fluxed powders has been used to produce novel amorphous/crystalline coatings with attractive wear properties [164]. Addition of Al_2O_3 to AlCoCrFeMnNi improves the thermal, oxidation, and mechanical properties of HEAs and indicated the potential of ODS HEAs as high-temperature coating material [44]. AlCoCrFeNi HEA powders have been explored for their electromagnetic interference properties and are shown to be an attractive candidate for microwave shielding applications [74, 128, 165].

Zhang et al. [73] have suggested that CoCrFeMoNi coatings can be a promising material for diamond tool applications, as they possess higher hardness (350–520 HV) than many of the conventional metal matrices used, e.g., Cobalite HDR (309 HV). MAed HEAs are also being explored to form composites and as additives in cermets. Addition of AlCoCrFeNi and AlCoCrFeNiTi powders to TiB_2 has been shown to exhibit excellent wettability, thereby lowering the sintering temperature required to process the ceramic composite [33, 82]. AlCoCrFeNi HEA was used as binders to fabricate Ti(C, N)-based cermets with simultaneous enhancement of hardness and toughness [166]. Mohanty et al. [86] demonstrated fine-scale precipitation in AlCoCuNiZn HEA, similar to that observed in superalloys and indicate potential of HEAs for high thermal stability. Cu matrix composites have been formed using addition of AlCoCrFeNi powders. Moravcik et al. [30] designed the TiC and $AlCoCrFeNiTi_{0.5}$ composites and obtained good mechanical properties (comparable to as-cast counterparts). Tan et al. [167] fabricated composites of amorphous $Al_{65}Cu_{16.5}Ti_{18.5}$ and crystalline (FCC + BCC) $Al_{0.6}CoCrFeNi$ HEA. These composites exhibited very high yield strength of 3.1 GPa but a low ductility. Yang et al. [168] reported the fabrication of nanoscale Al_2O_3-reinforced $Al_{0.4}CoCrFeNi_{1.2}Ti_{0.3}$ HEA composites, which possess major FCC phase along with minor fractions of BCC and Al_2O_3. The nanoscale Al_2O_3 provides precipitation strengthening to the alloy and seems to increase the fraction of nanotwins.

Challenges in processing of MAed HEAs

HEAs processed by MA offer exciting properties and promising applications. However, this synthesis route also faces some challenges, which need to be surmounted to further advance the production of nanocrystalline HEAs.

(i) Contamination from milling media is commonly observed during MA of HEAs [23]. The type and extent of contamination that occur during milling are chiefly determined by the milling media, PCA, duration of milling, speed of milling, and the characteristics of the materials milled [15]. It needs to be emphasized here that as far as MA of HEAs is concerned, there is no significant degradation of properties reported due to contamination. In fact, there have been numerous cases in which contaminants have proven beneficial. To illustrate, formation of TiO phase during SPS of MAed MoNbTaTiWV leads to excellent mechanical properties with a compressive yield strength of 2709 MPa, fracture strength of 3115 MPa, and fracture strain of 11.4% [98]. The oxide inclusions

https://doi.org/10.1557/jmr.2019.37 Published online by Cambridge University Press

© Materials Research Society 2019

formed during SPS of MoNbTaVW contribute to an ultra-high compressive strength obtained for the HEA [34]. Formation of V and Cr carbides in $CoCr_{0.5-x}CuFeNi_{1.5}V_x$ HEAs results in high compressive yield strength (>1 GPa) [119]. The real challenge lies in understanding the mechanism and controlling the extent of contamination, both of which have not been investigated in detail so far. The formation of Cr carbides is not only observed during consolidation of Cr-containing HEAs [12] but also during heat treatment [28] and prolonged milling [48]. Therefore, the source of carbon to form carbides during milling has been identified as PCA like toluene [39, 119, 169]. Vaidya et al. [39] have shown, using atom probe tomography, that Cr_7C_3 is present in CoCrFeMnNi powders milled for 15 h (Fig. 6), which hints toward the possibility of Cr_7C_3 formation at milling stage itself. However, the exact mechanism of decomposition of toluene to form C and subsequent reaction with Cr to form carbides has not been investigated yet. Meticulous analysis of milled powders and PCA at different stages of milling, using spectroscopic techniques like NMR, may shed light on the progression of toluene decomposition. While advantageous effects of contamination have been reported in the literature, its levels are often unsolicited and extent of it has not been controlled.

(ii) The vast compositional space of HEAs necessitated the development of computational tools for predicting the phase structure in these alloys using CALPHAD and first principle techniques. While the phase predictions are increasingly becoming accurate for HEAs produced by equilibrium methods, limited efforts have been made for the assessment of phases formed during MA or any other nonequilibrium process. Youssef et al. [95] showed that HCP phase formed after annealing of MAed AlLiMgScTi is in agreement with the DFT (density functional theory) calculations. Sun et al. [170] discussed in detail that the CALPHAD calculations for predicting phases formed during MA have low accuracy. Using the "liquid state" assumption, the calculated primary phase during solidification is considered as the major phase formed in the as-milled microstructure, but this treatment is rather tentative and not always valid. Elements like Mg and Si can cause the intermetallics to form during casting but get dissolved during MA to form simple solid solution structures (see, e.g., Tables I–III).

(iii) "Sluggish diffusion" was proposed as one of the core effects in HEAs. However, recent measurements using interdiffusion [171] and tracer diffusion techniques [172] have demonstrated that the diffusion in HEAs need not be assumed sluggish. The diffusion measurements for HEAs have been limited and only measured in cast alloys [173]. There have been no investigations of atomic transport in HEAs formed after MA and consolidation. A reliable measurement of diffusion in, say, SPSed HEAs, would prove critical to deepen the current understanding on phase stability and deformation behavior of these alloys. A major obstacle for dependable diffusivity measurements in

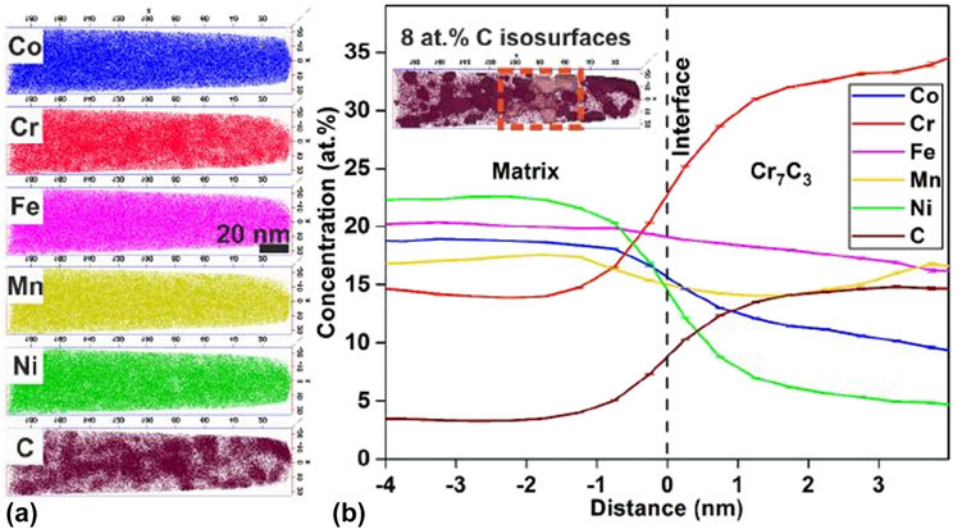


Figure 6: Atom probe tomography of CoCrFeMnNi HEA showing (a) elemental distribution of 15 h milled powder and (b) proximity histogram obtained from the highlighted region (dotted box) of the 8 at.% C isoconcentration surfaces revealing the presence of chromium carbide (Cr_7C_3) [39].

https://doi.org/10.1557/jmr.2019.37 Published online by Cambridge University Press

© Materials Research Society 2019

HEAs produced by MA is to get a contamination-free sample. Another challenge is to ensure the stability of nanostructured alloys at the temperatures and time used for diffusion annealing.

(iv) The milled powders are rarely used for any applications directly and often required to be either consolidated in form of dense pellets or sprayed as coatings. As noted in Tables I, II, and IV, phases formed during MA are often metastable and most of the HEAs undergo phase transitions to other solid solution structures and/or complex phases. Therefore, the choice of alloy compositions and milling conditions need to be made keeping in view the processing intended after MA. Some concerns like restricting grain growth of milled powders during consolidation, handling of nanocrystalline powders, maintaining an inert atmosphere during milling, and maintaining optimum milling schedule apply to MA of HEAs also, as it does for MA of conventional alloys.

(v) The multicomponent nature of HEAs makes it difficult to comprehend the alloying kinetics and delineate the influence of individual element on phase formation. This is further complicated for 3d transition element HEAs, when elements have similar atomic size and can possess similar structure and lattice parameters. For example, both Fe and Cr have BCC structure and similar lattice parameters. Furthermore, binaries like FCC CoNi and FeNi have similar unit cell dimensions as Ni, and therefore, their deconvolution XRD is not straightforward. The novel strategy of sequential alloying can prove useful to understand the role of alloying elements better. To illustrate, Vaidya et al. [48] demonstrated using sequential alloying strategy that BCC phase formed during MA of AlCoCrFeNi is FeCr rich and not disordered AlNi.

Conclusions

MA has increasingly been adopted as a popular route to synthesize nanocrystalline HEAs. The present review aimed to bring out key aspects of phase evolution, thermal stability, mechanical behavior, and functional properties of HEAs produced by MA and subsequent consolidation. Further intent was to discuss the potential applications of MA and the challenges, which lie ahead for the advancement of the field.

It has been shown that only solid solution phases are formed in HEAs after MA. Phase transformations to multiple solid solution phases and complex structures are observed on consolidation and annealing, which indicate the metastable nature of phases during MA. Several amorphous HEAs have been successfully produced by employing prolonged milling hours. The increasing configurational entropy does not significantly accelerate the alloying kinetics. The parametric approaches utilizing combination of thermodynamic and topological factors can be used to reasonably predict the phase structure of MAed HEAs. The effect of various alloying elements on phase evolution HEAs has also been discussed. Al has significant influence on phase formation as it dissolves in FCC phases at lower concentration and leads to the formation of B_2 phase when its content is high. Cr facilitates the evolution of BCC and σ phases. Cr-containing HEAs invariably show the appearance of carbides when milled powders are exposed at elevated temperatures. SPS is the most widely adopted technique to consolidate HEA powders, as it gives an excellent combination of densification and retention of nanocrystallinity. The dense pellets have been examined for various mechanical and functional properties. Multiple strengthening mechanisms contribute to the excellent compressive properties exhibited by SPSed HEAs; these include solid solution strengthening, precipitation hardening, and grain boundary and twin boundary (FCC phase) strengthening. The high hardness lends wear-resistant properties to HEAs, and few studies on corrosion behavior hint at protective nature of HEA coatings. Use of HEA powders in fabrication of cermets and development of HEA coatings and composites are some of the potential applications presented so far, for the alloys produced by MA.

Further advancement of HEAs processed by MA requires overcoming the challenges of reducing contamination, reliable phase predictions using CALPHAD, and first principle calculations, measuring kinetic properties and understanding the phase evolution during MA in greater detail. Use of high-purity inert atmosphere, milling of cast ingots, mechanically activated annealing, and sequential alloying methodology can help in achieving lower contamination levels. Production of contamination-free alloys will also facilitate the reliable measurements of diffusion and in turn provides comprehensive understanding of their phase stability and mechanical behavior. Careful optimization of milling parameters and sintering conditions can further help to control the microstructure of the HEAs and achieve enhanced properties.

References

1. **B.S. Murty, J.W. Yeh, and S. Ranganathan**: *High-Entropy Alloys* (Butterworth-Heinemann, London, UK, 2014).
2. **B. Cantor, I.T.H. Chang, P. Knight, and A.J.B. Vincent**: Microstructural development in equiatomic multicomponent alloys. *Mater. Sci. Eng., A* **375–377**, 213 (2004).
3. **J.W. Yeh, S.K. Chen, S.J. Lin, J.Y. Gan, T.S. Chin, T.T. Shun, C.H. Tsau, and S.Y. Chang**: Nanostructured high-entropy alloys with multiple principal elements: Novel alloy design concepts and outcomes. *Adv. Eng. Mater.* **6**, 299 (2004).

https://doi.org/10.1557/jmr.2019.37 Published online by Cambridge University Press

© Materials Research Society 2019

4. **Z. Li, K.G. Pradeep, Y. Deng, D. Raabe, and C.C. Tasan**: Metastable high-entropy dual-phase alloys overcome the strength–ductility trade-off. *Nature* **534**, 227 (2016).
5. **B. Gludovatz, A. Hohenwarter, D. Catoor, E.H. Chang, E. P. George, and R.O. Ritchie**: A fracture-resistant high-entropy alloy for cryogenic applications. *Science* **345**, 1153 (2014).
6. **M. Yang, X.J. Liu, H.H. Ruan, Y. Wu, H. Wang, and Z.P. Lu**: High thermal stability and sluggish crystallization kinetics of high-entropy bulk metallic glasses. *J. Appl. Phys.* **119**, 245112 (2016).
7. **T.M. Butler, J.P. Alfano, R.L. Martens, and M.L. Weaver**: High-temperature oxidation behavior of Al–Co–Cr–Ni–(Fe or Si) multicomponent high-entropy alloys. *JOM* **67**, 246 (2015).
8. **G. Laplanche, U.F. Volkert, G. Eggeler, and E.P. George**: Oxidation behavior of the CrMnFeCoNi high-entropy alloy. *Oxid. Met.* **85**, 629 (2016).
9. **J.H. Zhao, X.L. Ji, Y.P. Shan, Y. Fu, and Z. Yao**: On the microstructure and erosion–corrosion resistance of AlCrFeCoNiCu high-entropy alloy via annealing treatment. *Mater. Sci. Technol.* **32**, 1271 (2016).
10. **B. Schuh, F. Mendez-Martin, B. Völker, E.P. George, H. Clemens, R. Pippan, and A. Hohenwarter**: Mechanical properties, microstructure and thermal stability of a nanocrystalline CoCrFeMnNi high-entropy alloy after severe plastic deformation. *Acta Mater.* **96**, 258 (2015).
11. **Y. Zhang, T. Zuo, Y. Cheng, and P.K. Liaw**: High-entropy alloys with high saturation magnetization, electrical resistivity, and malleability. *Sci. Rep.* **3**, 1 (2013).
12. **S. Praveen, J. Basu, S. Kashyap, and R.S. Kottada**: Exceptional resistance to grain growth in nanocrystalline CoCrFeNi high entropy alloy at high homologous temperatures. *J. Alloys Compd.* **662**, 361 (2016).
13. **B.S. Murty and S. Ranganathan**: Novel materials synthesis by mechanical alloying/milling. *Int. Mater. Rev.* **43**, 101 (1998).
14. **J.S. Benjamin and T.E. Volin**: The mechanism of mechanical alloying. *Metall. Trans.* **5**, 1929 (1974).
15. **C. Suryanarayana**: Mechanical alloying and milling. *Prog. Mater. Sci.* **46**, 1 (2001).
16. **A.S.M. Ang, C.C. Berndt, M.L. Sesso, A. Anupam, S. Praveen, R.S. Kottada, and B.S. Murty**: Plasma-sprayed high entropy alloys: Microstructure and properties of AlCoCrFeNi and MnCoCrFeNi. *Metall. Mater. Trans. A* **46**, 791 (2014).
17. **S. Varalakshmi, M. Kamaraj, and B.S. Murty**: Synthesis and characterization of nanocrystalline AlFeTiCrZnCu high entropy solid solution by mechanical alloying. *J. Alloys Compd.* **460**, 253 (2008).
18. **D.B. Miracle and O.N. Senkov**: A critical review of high entropy alloys and related concepts. *Acta Mater.* **122**, 448 (2017).
19. **B.E. MacDonald, Z. Fu, B. Zheng, W. Chen, Y. Lin, F. Chen, L. Zhang, J. Ivanisenko, Y. Zhou, H. Hahn, and E.J. Lavernia**: Recent progress in high entropy alloy research. *JOM* **69**, 2024 (2017).
20. **Y. Shi, B. Yang, and P. Liaw**: Corrosion-resistant high-entropy alloys: A review. *Metals* **7**, 43 (2017).
21. **K. Guruvidyathri, K.C. Hari Kumar, J.W. Yeh, and B.S. Murty**: Topologically close-packed phase formation in high entropy alloys: A review of calphad and experimental results. *JOM* **69**, 2113 (2017).
22. **E.J. Pickering and N.G. Jones**: High-entropy alloys: A critical assessment of their founding principles and future prospects. *Int. Mater. Rev.* **61**, 183 (2016).
23. **A.S. Sharma, S. Yadav, K. Biswas, and B. Basu**: High-entropy alloys and metallic nanocomposites: Processing challenges, microstructure development and property enhancement. *Mater. Sci. Eng., R* **131**, 1 (2018).
24. **C.C. Koch**: Nanocrystalline high-entropy alloys. *J. Mater. Res.* **32**, 3435 (2017).
25. **C.D. Gómez-Esparza, F. Baldenebro-López, L. González-Rodelas, J. Baldenebro-López, and R. Martínez-Sánchez**: Series of nanocrystalline NiCoAlFe(Cr, Cu, Mo, Ti) high-entropy alloys produced by mechanical alloying. *Mater. Res.* **19**, 39 (2016).
26. **C. Sun, P. Li, S. Xi, Y. Zhou, S. Li, and X. Yang**: A new type of high entropy alloy composite $Fe_{18}Ni_{23}Co_{25}Cr_{21}Mo_8WNb_3C_2$ prepared by mechanical alloying and hot pressing sintering. *Mater. Sci. Eng., A* **728**, 144 (2018).
27. **Ł. Rogal, D. Kalita, A. Tarasek, P. Bobrowski, and F. Czerwinski**: Effect of SiC nano-particles on microstructure and mechanical properties of the CoCrFeMnNi high entropy alloy. *J. Alloys Compd.* **708**, 344 (2017).
28. **A.J. Zaddach, C. Niu, A.A. Oni, M. Fan, J.M. LeBeau, D. L. Irving, and C.C. Koch**: Structure and magnetic properties of a multi-principal element Ni–Fe–Cr–Co–Zn–Mn alloy. *Intermetallics* **68**, 107 (2016).
29. **Z. Fu, W. Chen, S. Fang, and X. Li**: Effect of Cr addition on the alloying behavior, microstructure and mechanical properties of twinned $CoFeNiAl_{0.5}Ti_{0.5}$ alloy. *Mater. Sci. Eng., A* **597**, 204 (2014).
30. **I. Moravcik, J. Cizek, P. Gavendova, S. Sheikh, S. Guo, and I. Dlouhy**: Effect of heat treatment on microstructure and mechanical properties of spark plasma sintered $AlCoCrFeNiTi_{0.5}$ high entropy alloy. *Mater. Lett.* **174**, 53 (2016).
31. **B. Wu, W. Chen, Z. Jiang, Z. Chen, and Z. Fu**: Influence of Ti addition on microstructure and mechanical behavior of a FCC-based $Fe_{30}Ni_{30}Co_{30}Mn_{10}$ alloy. *Mater. Sci. Eng., A* **676**, 492 (2016).
32. **A. Dwivedi, C.C. Koch, and K.V. Rajulapati**: On the single phase fcc solid solution in nanocrystalline Cr–Nb–Ti–V–Zn high-entropy alloy. *Mater. Lett.* **183**, 44 (2016).
33. **S. Zhang, Y. Sun, B. Ke, Y. Li, W. Ji, W. Wang, and Z. Fu**: Preparation and characterization of TiB_2-(supra-nano-dual-phase) high-entropy alloy cermet by spark plasma sintering. *Metals* **8**, 58 (2018).

https://doi.org/10.1557/jmr.2019.37 Published online by Cambridge University Press

© Materials Research Society 2019

34. **B. Kang, J. Lee, H.J. Ryu, and S.H. Hong**: Ultra-high strength WNbMoTaV high-entropy alloys with fine grain structure fabricated by powder metallurgical process. *Mater. Sci. Eng., A* **712**, 616 (2018).
35. **W. Ge, B. Wu, S. Wang, S. Xu, C. Shang, Z. Zhang, and Y. Wang**: Characterization and properties of CuZrAlTiNi high entropy alloy coating obtained by mechanical alloying and vacuum hot pressing sintering. *Adv. Powder Technol.* **28**, 2556 (2017).
36. **Z. Fu, W. Chen, Z. Jiang, B.E. MacDonald, Y. Lin, F. Chen, L. Zhang, and E.J. Lavernia**: Influence of Cr removal on the microstructure and mechanical behaviour of a high-entropy $Al_{0.8}Ti_{0.2}$CoNiFeCr alloy fabricated by powder metallurgy. *Powder Metall.* **5899**, 1 (2018).
37. **F. Salemi, M.H. Abbasi, and F. Karimzadeh**: Synthesis and thermodynamic analysis of nanostructured CuNiCoZnAl high entropy alloy produced by mechanical alloying. *J. Alloys Compd.* **685**, 278 (2016).
38. **X.R. Tan, G.P. Zhang, Q. Zhi, and Z.X. Liu**: Effects of milling on the microstructure and hardness of $Al_2NbTi_3V_2Zr$ high-entropy alloy. *Mater. Des.* **109**, 27 (2016).
39. **M. Vaidya, A. Karati, A. Marshal, K.G. Pradeep, and B. S. Murty**: Phase evolution and stability of nanocrystalline CoCrFeNi and CoCrFeMnNi high entropy alloys. *J. Alloys Compd.* **770**, 1004 (2019).
40. **W. Ji, W. Wang, H. Wang, J. Zhang, Y. Wang, F. Zhang, and Z. Fu**: Alloying behavior and novel properties of CoCrFeNiMn high-entropy alloy fabricated by mechanical alloying and spark plasma sintering. *Intermetallics* **56**, 24 (2014).
41. **J. Xu, Z.F. Zhao, and Y. Wang**: Effect of annealing treatment on the microstructure and magnetic properties of FeSiBAlNi(C, Ce) high entropy alloys. *Mater. Sci. Forum* **849**, 52 (2016).
42. **H.L. Wang, T.X. Gao, J.Z. Niu, P.J. Shi, J. Xu, and Y. Wang**: Microstructure, thermal properties, and corrosion behaviors of FeSiBAlNi alloy fabricated by mechanical alloying and spark plasma sintering. *Int. J. Miner., Metall. Mater.* **23**, 77 (2016).
43. **E. Colombini, R. Rosa, L. Trombi, M. Zadra, A. Casagrande, and P. Veronesi**: High entropy alloys obtained by field assisted powder metallurgy route: SPS and microwave heating. *Mater. Chem. Phys.* **210**, 78 (2018).
44. **H. Prasad, S. Singh, and B.B. Panigrahi**: Mechanical activated synthesis of alumina dispersed FeNiCoCrAlMn high entropy alloy. *J. Alloys Compd.* **692**, 720 (2017).
45. **B. Kang, J. Lee, H.J. Ryu, and S.H. Hong**: Microstructure, mechanical property and Hall–Petch relationship of a light-weight refractory $Al_{0.1}$CrNbVMo high entropy alloy fabricated by powder metallurgical process. *J. Alloys Compd.* **767**, 1012 (2018).
46. **N. Kumar, C.S. Tiwary, and K. Biswas**: Preparation of nanocrystalline high-entropy alloys via cryomilling of cast ingots. *J. Mater. Sci.* **53**, 13411 (2018).
47. **S. Varalakshmi, M. Kamaraj, and B.S. Murty**: Formation and stability of equiatomic and nonequiatomic nanocrystalline CuNiCoZnAlTi high-entropy alloys by mechanical alloying. *Metall. Mater. Trans. A* **41**, 2703 (2010).
48. **M. Vaidya, A. Prasad, A. Parakh, and B.S. Murty**: Influence of sequence of elemental addition on phase evolution in nanocrystalline AlCoCrFeNi: Novel approach to alloy synthesis using mechanical alloying. *Mater. Des.* **126**, 37 (2017).
49. **Y. Xie, H. Cheng, Q. Tang, W. Chen, W. Chen, and P. Dai**: Effects of N addition on microstructure and mechanical properties of CoCrFeNiMn high entropy alloy produced by mechanical alloying and vacuum hot pressing sintering. *Intermetallics* **93**, 228 (2018).
50. **H. Cheng, W. Chen, X. Liu, Q. Tang, Y. Xie, and P. Dai**: Effect of Ti and C additions on the microstructure and mechanical properties of the FeCoCrNiMn high-entropy alloy. *Mater. Sci. Eng., A* **719**, 192 (2018).
51. **S. Varalakshmi, M. Kamaraj, and B.S. Murty**: Processing and properties of nanocrystalline CuNiCoZnAlTi high entropy alloys by mechanical alloying. *Mater. Sci. Eng., A* **527**, 1027 (2010).
52. **Z. Fu, W. Chen, Z. Chen, H. Wen, and E.J. Lavernia**: Influence of Ti addition and sintering method on microstructure and mechanical behavior of a medium-entropy $Al_{0.6}$CoNiFe alloy. *Mater. Sci. Eng., A* **619**, 137 (2014).
53. **V. Shivam, J. Basu, Y. Shadangi, M.K. Singh, and N.K. K. Mukhopadhyay**: Mechano-chemical synthesis, thermal stability and phase evolution in AlCoCrFeNiMn high entropy alloy. *J. Alloys Compd.* **757**, 87 (2018).
54. **S. Varalakshmi, G. Appa Rao, M. Kamaraj, and B.S. Murty**: Hot consolidation and mechanical properties of nanocrystalline equiatomic AlFeTiCrZnCu high entropy alloy after mechanical alloying. *J. Mater. Sci.* **45**, 5158 (2010).
55. **M. Omori**: Sintering, consolidation, reaction and crystal growth by the spark plasma system (SPS). *Mater. Sci. Eng., A* **287**, 183 (2000).
56. **M. Murali, S.P. Kumaresh Babu, J. Majhi, A. Vallimanalan, and R. Mahendran**: Processing and characterisation of nano crystalline AlCoCrCuFeTi$_x$ high-entropy alloy. *Powder Metall.* **61**, 139 (2018).
57. **S. Praveen, B.S. Murty, and R.S. Kottada**: Alloying behavior in multi-component AlCoCrCuFe and NiCoCrCuFe high entropy alloys. *Mater. Sci. Eng., A* **534**, 83 (2012).
58. **S-H. Joo, H. Kato, M.J. Jang, J. Moon, E.B. Kim, S-J. Hong, and H.S. Kim**: Structure and properties of ultrafine-grained CoCrFeMnNi high-entropy alloys produced by mechanical alloying and spark plasma sintering. *J. Alloys Compd.* **698**, 591 (2017).
59. **P. Wang, H. Cai, and X. Cheng**: Effect of Ni/Cr ratio on phase, microstructure and mechanical properties of $Ni_xCoCuFeCr_{2-x}$ (x = 1.0, 1.2, 1.5, 1.8 mol) high entropy alloys. *J. Alloys Compd.* **662**, 20 (2016).

https://doi.org/10.1557/jmr.2019.37 Published online by Cambridge University Press

© Materials Research Society 2019

60. **M. Vaidya, K.G. Pradeep, B.S. Murty, G. Wilde, and S. V. Divinski**: Radioactive isotopes reveal a non sluggish kinetics of grain boundary diffusion in high entropy alloys. *Sci. Rep.* **7**, 1 (2017).
61. **S. Praveen, B.S. Murty, and R.S. Kottada**: Phase evolution and densification behavior of nanocrystalline multicomponent high entropy alloys during spark plasma sintering. *JOM* **65**, 1797 (2013).
62. **S. Praveen, A. Anupam, T. Sirasani, B.S. Murty, and R. S. Kottada**: Characterization of oxide dispersed AlCoCrFe high entropy alloy synthesized by mechanical alloying and spark plasma sintering. *Trans. Indian Inst. Met.* **66**, 369 (2013).
63. **R.B. Mane, Y. Rajkumar, and B.B. Panigrahi**: Sintering mechanism of CoCrFeMnNi high-entropy alloy powders. *Powder Metall.* **61**, 131 (2018).
64. **R.B. Mane and B.B. Panigrahi**: Sintering mechanisms of mechanically alloyed CoCrFeNi high-entropy alloy powders. *J. Mater. Res.* **33**, 3321 (2018).
65. **R.B. Mane and B.B. Panigrahi**: Comparative study on sintering kinetics of as-milled and annealed CoCrFeNi high entropy alloy powders. *Mater. Chem. Phys.* **210**, 49 (2018).
66. **R.B. Mane and B.B. Panigrahi**: Effect of alloying order on non-isothermal sintering kinetics of mechanically alloyed high entropy alloy powders. *Mater. Lett.* **217**, 131 (2018).
67. **E. Colombini, M. Lassinantti Gualtieri, R. Rosa, F. Tarterini, M. Zadra, A. Casagrande, and P. Veronesi**: SPS-assisted synthesis of SIC_p reinforced high entropy alloys: Reactivity of SIC and effects of pre-mechanical alloying and post-annealing treatment. *Powder Metall.* **61**, 64 (2018).
68. **Z. Liu, Y. Lei, C. Gray, and G. Wang**: Examination of solid-solution phase formation rules for high entropy alloys from atomistic Monte Carlo simulations. *JOM* **67**, 2364 (2015).
69. **Y. Zhang and Y.J. Zhou**: Solid solution formation criteria for high entropy alloys. *Mater. Sci. Forum* **561–565**, 1337 (2007).
70. **S. Guo, C. Ng, J. Lu, and C.T. Liu**: Effect of valence electron concentration on stability of fcc or bcc phase in high entropy alloys. *J. Appl. Phys.* **109**, 103505 (2011).
71. **A. Kumar, P. Dhekne, A.K. Swarnakar, and M.K. Chopkar**: Analysis of Si addition on phase formation in $AlCoCrCuFeNiSi_x$ high entropy alloys. *Mater. Lett.* **188**, 73 (2017).
72. **S. Mohanty, T.N. Maity, S. Mukhopadhyay, S. Sarkar, N. P. Gurao, S. Bhowmick, and K. Biswas**: Powder metallurgical processing of equiatomic AlCoCrFeNi high entropy alloy: Microstructure and mechanical properties. *Mater. Sci. Eng., A* **679**, 299 (2017).
73. **M. Zhang, W. Zhang, Y. Liu, B. Liu, and J. Wang**: FeCoCrNiMo high-entropy alloys prepared by powder metallurgy processing for diamond tool applications. *Powder Metall.* **61**, 123 (2018).
74. **Y. Zhang, B. Zhang, K. Li, G.L. Zhao, and S.M. Guo**: Electromagnetic interference shielding effectiveness of high entropy AlCoCrFeNi alloy powder laden composites. *J. Alloys Compd.* **734**, 220 (2018).
75. **J. Chen, P. Niu, T. Wei, L. Hao, Y. Liu, X. Wang, and Y. Peng**: Fabrication and mechanical properties of AlCoNiCrFe high-entropy alloy particle reinforced Cu matrix composites. *J. Alloys Compd.* **649**, 630 (2015).
76. **V. Shivam, J. Basu, Y. Shadangi, M.K. Singh, and N. K. Mukhoupadhyay**: Mechano-chemical synthesis, thermal stability and phase evolution in AlCoCrFeNiMn high entropy alloy. *J. Alloys Compd.* **757**, 20 (2016).
77. **S. Praveen, A. Anupam, R. Tilak, and R.S. Kottada**: Phase evolution and thermal stability of AlCoCrFe high entropy alloy with carbon as unsolicited addition from milling media. *Mater. Chem. Phys.* **210**, 57 (2018).
78. **R.M. Pohan, B. Gwalani, J. Lee, T. Alam, J.Y. Hwang, H.J. Ryu, R. Banerjee, and S.H. Hong**: Microstructures and mechanical properties of mechanically alloyed and spark plasma sintered $Al_{0.3}CoCrFeMnNi$ high entropy alloy. *Mater. Chem. Phys.* **210**, 62 (2018).
79. **M. Vaidya, S. Armugam, S. Kashyap, and B.S.S. Murty**: Amorphization in equiatomic high entropy alloys. *J. Non-Cryst. Solids* **413**, 8 (2015).
80. **Z. Fu, W. Chen, H. Wen, D. Zhang, Z. Chen, B. Zheng, Y. Zhou, and E.J. Lavernia**: Microstructure and strengthening mechanisms in an FCC structured single-phase nanocrystalline $Co_{25}Ni_{25}Fe_{25}Al_{7.5}Cu_{17.5}$ high-entropy alloy. *Acta Mater.* **107**, 59 (2016).
81. **L.H. Tian, W. Xiong, C. Liu, S. Lu, and M. Fu**: Microstructure and wear behavior of atmospheric plasma-sprayed AlCoCrFeNiTi high-entropy alloy coating. *J. Mater. Eng. Perform.* **25**, 5513 (2016).
82. **W. Ji, J. Zhang, W. Wang, H. Wang, F. Zhang, Y. Wang, and Z. Fu**: Fabrication and properties of TiB_2-based cermets by spark plasma sintering with CoCrFeNiTiAl high-entropy alloy as sintering aid. *J. Eur. Ceram. Soc.* **35**, 879 (2014).
83. **H. Hadraba, Z. Chlup, A. Dlouhy, F. Dobes, P. Roupcova, M. Vilemova, and J. Matejicek**: Oxide dispersion strengthened CoCrFeNiMn high-entropy alloy. *Mater. Sci. Eng., A* **689**, 252 (2017).
84. **Y. Liu, J. Wang, Q. Fang, B. Liu, Y. Wu, and S. Chen**: Preparation of superfine-grained high entropy alloy by spark plasma sintering gas atomized powder. *Intermetallics* **68**, 16 (2016).
85. **M. Murali, S.P.K. Babu, B.J. Krishna, and A. Vallimanalan**: Synthesis and characterization of $AlCoCrCuFeZn_x$ high-entropy alloy by mechanical alloying. *Prog. Nat. Sci.: Mater. Int.* **26**, 380 (2016).
86. **S. Mohanty, N.P. Gurao, and K. Biswas**: Sinter ageing of equiatomic $Al_{20}Co_{20}Cu_{20}Zn_{20}Ni_{20}$ high entropy alloy via mechanical alloying. *Mater. Sci. Eng., A* **617**, 211 (2014).
87. **A.I. Yurkova, V.V. Chernyavskii, and V.F. Gorban**: Structure and mechanical properties of high-entropy AlCuNiFeTi and AlCuNiFeCr alloys produced by mechanical activation followed

https://doi.org/10.1557/jmr.2019.37 Published online by Cambridge University Press

© Materials Research Society 2019

by pressure sintering. *Powder Metall. Met. Ceram.* **55**, 152 (2016).

88. **R.F. Zhao, B. Ren, G.P. Zhang, Z.X. Liu, and J. jian Zhang**: Effect of Co content on the phase transition and magnetic properties of Co_xCrCuFeMnNi high-entropy alloy powders. *J. Magn. Magn. Mater.* **468**, 14 (2018).
89. **Y. Tong, P. Qi, X. Liang, Y. Chen, Y. Hu, and Z. Hu**: Different-shaped ultrafine MoNbTaW HEA powders prepared via mechanical alloying. *Materials* **10**, 1 (2018).
90. **A. Kumar, A.K.A.K. Swarnakar, and M. Chopkar**: Phase evolution and mechanical properties of AlCoCrFeNiSi_x high-entropy alloys synthesized by mechanical alloying and spark plasma sintering. *J. Mater. Eng. Perform.* **27**, 3304 (2018).
91. **H. Cheng, X. Liu, Q. Tang, W. Wang, X. Yan, and P. Dai**: Microstructure and mechanical properties of FeCoCrNiMnAl_x high-entropy alloys prepared by mechanical alloying and hot-pressed sintering. *J. Alloys Compd.* **775**, 742 (2019).
92. **W. Guo, B. Liu, Y. Liu, T. Li, A. Fu, Q. Fang, and Y. Nie**: Microstructures and mechanical properties of ductile NbTaTiV refractory high entropy alloy prepared by powder metallurgy. *J. Alloys Compd.* **776**, 428 (2019).
93. **D. Oleszak, A. Antolak-Dudka, and T. Kulik**: High entropy multicomponent WMoNbZrV alloy processed by mechanical alloying. *Mater. Lett.* **232**, 160 (2018).
94. **V. Shivam, J. Basu, V.K. Pandey, Y. Shadangi, and N. K. Mukhopadhyay**: Alloying behaviour, thermal stability and phase evolution in quinary AlCoCrFeNi high entropy alloy. *Adv. Powder Technol.* **29**, 2221 (2018).
95. **K.M. Youssef, A.J. Zaddach, C. Niu, D.L. Irving, and C. C. Koch**: A novel low-density, high-hardness, high-entropy alloy with close-packed single-phase nanocrystalline structures. *Mater. Res. Lett.* **3**, 95 (2014).
96. **Q. Yang, Y. Tang, Y. Wen, Q. Zhang, D. Deng, and X. Nai**: Microstructures and properties of CoCrCuFeNiMo_x high-entropy alloys fabricated by mechanical alloying and spark plasma sintering. *Powder Metall.* **61**, 115 (2018).
97. **L. Tian, M. Fu, and W. Xiong**: Microstructural evolution of AlCoCrFeNiSi high-entropy alloy powder during mechanical alloying and its coating performance. *Materials* **11**, 320 (2018).
98. **Y. Long, K. Su, J. Zhang, X. Liang, H. Peng, and X. Li**: Enhanced strength of a mechanical alloyed NbMoTaWVTi refractory high entropy alloy. *Materials* **11**, 1 (2018).
99. **D. Kumar, O. Maulik, S. Kumar, Y.V.S.S. Prasad, and V. Kumar**: Phase and thermal study of equiatomic AlCuCrFeMnW high entropy alloy processed via spark plasma sintering. *Mater. Chem. Phys.* **210**, 71 (2018).
100. **K.B. Zhang, Z.Y. Fu, J.Y. Zhang, W.M. Wang, S.W. Lee, and K. Niihara**: Characterization of nanocrystalline CoCrFeNiTiAl high-entropy solid solution processed by mechanical alloying. *J. Alloys Compd.* **495**, 33 (2010).
101. **S. Praveen, B.S. Murty, and R.S. Kottada**: Effect of molybdenum and niobium on the phase formation and hardness of nanocrystalline CoCrFeNi high entropy alloys. *J. Nanosci. Nanotechnol.* **14**, 8106 (2014).
102. **F. Yuhu, Z. Yunpeng, G. Hongyan, S. Huimin, and H. Li**: AlNiCrFe$_x$$Mo_{0.2}$CoCu high entropy alloys prepared by powder metallurgy. *Rare Met. Mater. Eng.* **42**, 1127 (2013).
103. **Z.Q. Fu, W.P. Chen, S.C. Fang, D.Y. Zhang, H.Q. Xiao, and D. Z. Zhu**: Alloying behavior and deformation twinning in a CoNiFeCr$Al_{0.6}$$Ti_{0.4}$ high entropy alloy processed by spark plasma sintering. *J. Alloys Compd.* **553**, 316 (2013).
104. **Z. Fu, W. Chen, H. Xiao, L. Zhou, D. Zhu, and S. Yang**: Fabrication and properties of nanocrystalline $Co_{0.5}$FeNiCr$Ti_{0.5}$ high entropy alloy by MA-SPS technique. *Mater. Des.* **44**, 535 (2013).
105. **D. Kumar, O. Maulik, A.S. Bagri, Y.V.S.S. Prasad, and V. Kumar**: Microstructure and characterization of mechanically alloyed equiatomic AlCuCrFeMnW high entropy alloy. *Mater. Today: Proc.* **3**, 2926 (2016).
106. **N.T.B.N. Koundinya, C. Sajith Babu, K. Sivaprasad, P. Susila, N. Kishore Babu, and J. Baburao**: Phase evolution and thermal analysis of nanocrystalline AlCrCuFeNiZn high entropy alloy produced by mechanical alloying. *J. Mater. Eng. Perform.* **22**, 3077 (2013).
107. **S. Mridha, S. Samal, P.Y. Khan, K. Biswas, and Govind**: Processing and consolidation of nanocrystalline Cu–Zn–Ti–Fe–Cr high-entropy alloys via mechanical alloying. *Metall. Mater. Trans. A* **44**, 4532 (2013).
108. **N.H. Tariq, M. Naeem, B.A. Hasan, J.I. Akhter, and M. Siddique**: Effect of W and Zr on structural, thermal and magnetic properties of AlCoCrCuFeNi high entropy alloy. *J. Alloys Compd.* **556**, 79 (2013).
109. **F. Průša, A. Šenková, V. Kučera, J. Čapek, and D. Vojtěch**: Properties of a high-strength ultrafine-grained CoCrFeNiMn high-entropy alloy prepared by short-term mechanical alloying and spark plasma sintering. *Mater. Sci. Eng., A* **734**, 341 (2018).
110. **S. Fang, W. Chen, and Z. Fu**: Microstructure and mechanical properties of twinned $Al_{0.5}$CrFeNi$Co_{0.3}C_{0.2}$ high entropy alloy processed by mechanical alloying and spark plasma sintering. *Mater. Des.* **54**, 973 (2014).
111. **C. Wang, W. Ji, and Z. Fu**: Mechanical alloying and spark plasma sintering of CoCrFeNiMnAl high-entropy alloy. *Adv. Powder Technol.* **25**, 1334 (2014).
112. **Z. Fu, W. Chen, H. Wen, Z. Chen, and E.J. Lavernia**: Effects of Co and sintering method on microstructure and mechanical behavior of a high-entropy $Al_{0.6}$NiFeCrCo alloy prepared by powder metallurgy. *J. Alloys Compd.* **646**, 175 (2015).
113. **Z. Chen, W. Chen, B. Wu, X. Cao, L. Liu, and Z. Fu**: Effects of Co and Ti on microstructure and mechanical behavior of $Al_{0.75}$FeNiCrCo high entropy alloy prepared by mechanical

https://doi.org/10.1557/jmr.2019.37 Published online by Cambridge University Press

© Materials Research Society 2019

alloying and spark plasma sintering. *Mater. Sci. Eng., A* **648**, 217 (2015).

114. **F.J. Baldenebro-Lopez, J.M. Herrera-Ramírez, S.P. Arredondo-Rea, C.D. Gómez-Esparza, and R. Martínez-Sánchez**: Simultaneous effect of mechanical alloying and arc-melting processes in the microstructure and hardness of an AlCoFeMoNiTi high-entropy alloy. *J. Alloys Compd.* **643**, S250 (2015).
115. **Z. Fu, W. Chen, H. Wen, S. Morgan, F. Chen, B. Zheng, Y. Zhou, L. Zhang, and E.J. Lavernia**: Microstructure and mechanical behavior of a novel $Co_{20}Ni_{20}Fe_{20}Al_{20}Ti_{20}$ alloy fabricated by mechanical alloying and spark plasma sintering. *Mater. Sci. Eng., A* **644**, 10 (2015).
116. **H. Khanchandani, P. Sharma, R. Kumar, O. Maulik, and V. Kumar**: Effect of sintering on phase evolution in $AlMgFeCuCrNi_{4.75}$ high entropy alloy. *Adv. Powder Technol.* **27**, 289 (2016).
117. **I. Moravcik, J. Cizek, J. Zapletal, Z. Kovacova, J. Vesely, P. Minarik, M. Kitzmantel, E. Neubauer, and I. Dlouhy**: Microstructure and mechanical properties of $Ni_{1.5}Co_{1.5}CrFeTi_{0.5}$ high entropy alloy fabricated by mechanical alloying and spark plasma sintering. *Mater. Des.* **119**, 141 (2017).
118. **P.F. Yu, L.J. Zhang, H. Cheng, H. Zhang, M.Z. Ma, Y.C. Li, G. Li, P.K. Liaw, and R.P. Liu**: The high-entropy alloys with high hardness and soft magnetic property prepared by mechanical alloying and high-pressure sintering. *Intermetallics* **70**, 82 (2016).
119. **P. Wang, H. Cai, S. Zhou, and L. Xu**: Processing, microstructure and properties of $Ni_{1.5}CoCuFeCr_{0.5-x}V_x$ high entropy alloys with carbon introduced from process control agent. *J. Alloys Compd.* **695**, 462 (2017).
120. **C. Shang, E. Axinte, J. Sun, X. Li, P. Li, J. Du, P. Qiao, and Y. Wang**: $CoCrFeNi(W_{1-x}Mo_x)$ high-entropy alloy coatings with excellent mechanical properties and corrosion resistance prepared by mechanical alloying and hot pressing sintering. *Mater. Des.* **117**, 193 (2017).
121. **O. Maulik, D. Kumar, S. Kumar, D.M. Fabijanic, and V. Kumar**: Structural evolution of spark plasma sintered $AlFeCuCrMg_x$ ($x = 0, 0.5, 1, 1.7$) high entropy alloys. *Intermetallics* **77**, 46 (2016).
122. **O. Maulik and V. Kumar**: Synthesis of $AlFeCuCrMg_x$ ($x = 0, 0.5, 1, 1.7$) alloy powders by mechanical alloying. *Mater. Charact.* **110**, 116 (2015).
123. **B. Zhang, Y. Duan, Y. Cui, G. Ma, T. Wang, and X. Dong**: A new mechanism for improving electromagnetic properties based on tunable crystallographic powders. *RSC Adv.* **8**, 14936 (2018).
124. **I. Moravcik, L. Gouvea, V. Hornik, Z. Kovacova, M. Kitzmantel, E. Neubauer, and I. Dlouhy**: Synergic strengthening by oxide and coherent precipitate dispersions in high-entropy alloy prepared by powder metallurgy. *Scr. Mater.* **157**, 24 (2018).
125. **F. Alijani, M. Reihanian, and K. Gheisari**: Study on phase formation in magnetic FeCoNiMnV high entropy alloy produced by mechanical alloying. *J. Alloys Compd.* **773**, 623 (2019).
126. **S. Nam, M.J. Kim, J.Y. Hwang, and H. Choi**: Strengthening of $Al_{0.15}CoCrCuFeNiTi_x$–C ($x = 0, 1, 2$) high-entropy alloys by grain refinement and using nanoscale carbides via powder metallurgical route. *J. Alloys Compd.* **762**, 29 (2018).
127. **S. Yadav, S. Sarkar, A. Aggarwal, A. Kumar, and K. Biswas**: Wear and mechanical properties of novel $(CuCrFeTiZn)_{100-x}Pb_x$ high entropy alloy composite via mechanical alloying and spark plasma sintering. *Wear* **410–411**, 93 (2018).
128. **B. Zhang, Y. Duan, Y. Cui, G. Ma, T. Wang, and X. Dong**: Improving electromagnetic properties of $FeCoNiSi_{0.4}Al_{0.4}$ high entropy alloy powders via their tunable aspect ratio and elemental uniformity. *Mater. Des.* **149**, 173 (2018).
129. **H. Baker and H. Okamoto**: *ASM Handbook: Alloy Phase Diagrams*, Vol. **3** (ASM International, Materials Park, Ohio, 1992); p. 1741.
130. **M. Vaidya, K. Guruvidyathri, and B.S. Murty**: Phase formation and thermal stability of CoCrFeNi and CoCrFeMnNi equiatomic high entropy alloys. *J. Alloys Compd.* **774**, 856 (2019).
131. **Y.L. Chen, Y.H. Hu, C.A. Hsieh, J.W. Yeh, and S.K. Chen**: Competition between elements during mechanical alloying in an octonary multi-principal-element alloy system. *J. Alloys Compd.* **481**, 768 (2009).
132. **L. Ma, L. Wang, T. Zhang, and A. Inoue**: Bulk glass formation of Ti–Zr–Hf–Cu–M (M = Fe, Co, Ni) alloys. *Mater. Trans.* **43**, 277 (2002).
133. **W. Ge, Y. Wang, C. Shang, Z. Zhang, and Y. Wang**: Microstructures and properties of equiatomic CuZr and CuZrAlTiNi bulk alloys fabricated by mechanical alloying and spark plasma sintering. *J. Mater. Sci.* **52**, 5726 (2017).
134. **Y.L. Chen, C.W. Tsai, C.C. Juan, M.H. Chuang, J.W. Yeh, T. S. Chin, and S.K. Chen**: Amorphization of equimolar alloys with HCP elements during mechanical alloying. *J. Alloys Compd.* **506**, 210 (2010).
135. **Y.L. Chen, Y.H. Hu, C.W. Tsai, C.A. Hsieh, S.W. Kao, J. W. Yeh, T.S. Chin, and S.K. Chen**: Alloying behavior of binary to octonary alloys based on Cu–Ni–Al–Co–Cr–Fe–Ti–Mo during mechanical alloying. *J. Alloys Compd.* **477**, 696 (2009).
136. **Y.L. Chen, Y.H. Hu, C.W. Tsai, J.W. Yeh, S.K. Chen, and S. Y. Chang**: Structural evolution during mechanical milling and subsequent annealing of Cu–Ni–Al–Co–Cr–Fe–Ti alloys. *Mater. Chem. Phys.* **118**, 354 (2009).
137. **A.W. Weeber and H. Bakker**: Amorphization by ball milling. *A review. Physica B* **153**, 93–135 (1988).
138. **W. Wang, B. Li, S. Zhai, J. Xu, Z. Niu, J. Xu, and Y. Wang**: Alloying behavior and properties of $FeSiBAlNiCo_x$ high entropy alloys fabricated by mechanical alloying and spark plasma sintering. *Met. Mater. Int.* **24**, 1112–1119 (2018).

https://doi.org/10.1557/jmr.2019.37 Published online by Cambridge University Press

© Materials Research Society 2019

139. **L.C. Zhang, K.B. Kim, P. Yu, W.Y. Zhang, U. Kunz, and J. Eckert**: Amorphization in mechanically alloyed (Ti, Zr, Nb)–(Cu, Ni)–Al equiatomic alloys. *J. Alloys Compd.* **428**, 157 (2007).

140. **H-V. Nguyen, J-S. Kim, Y-S. Kwon, and J-C. Kim**: Amorphous Ti–Cu–Ni–Al alloys prepared by mechanical alloying. *J. Mater. Sci.* **44**, 2700 (2009).

141. **V.K. Portnoi, A.V. Leonov, S.E. Filippova, A.N. Streletskii, and A.I. Logacheva**: Mechanochemical synthesis and heating-induced transformations of a high-entropy Cr–Fe–Co–Ni–Al–Ti alloy. *Inorg. Mater.* **50**, 1202 (2014).

142. **J. Wang, Z. Zheng, J. Xu, and Y. Wang**: Microstructure and magnetic properties of mechanically alloyed FeSiBAlNi(Nb) high entropy alloys. *J. Magn. Magn. Mater.* **355**, 58 (2014).

143. **J. Xu, C. Shang, W. Ge, H. Jia, P.K. Liaw, and Y. Wang**: Effects of elemental addition on the microstructure, thermal stability, and magnetic properties of the mechanically alloyed FeSiBAlNi high entropy alloys. *Adv. Powder Technol.* **27**, 1418 (2016).

144. **J. Xu, E. Axinte, Z. Zhao, and Y. Wang**: Effect of C and Ce addition on the microstructure and magnetic property of the mechanically alloyed FeSiBAlNi high entropy alloys. *J. Magn. Magn. Mater.* **414**, 59 (2016).

145. **W. juan Ge, X. ting Li, P. Li, P. chao Qiao, J. wei Du, S. Xu, and Y. Wang**: Microstructures and properties of CuZrAl and CuZrAlTi medium entropy alloys prepared by mechanical alloying and spark plasma sintering. *J. Iron Steel Res. Int.* **24**, 448 (2017).

146. **X. Zhu, X. Zhou, S. Yu, C. Wei, J. Xu, and Y. Wang**: Effects of annealing on the microstructure and magnetic property of the mechanically alloyed FeSiBAlNiM (M = Co, Cu, Ag) amorphous high entropy alloys. *J. Magn. Magn. Mater.* **430**, 59 (2017).

147. **S.R. Shatynski**: The thermochemistry of transition metal carbides. *Oxid. Met.* **13**, 105 (1979).

148. **K.B. Zhang, Z.Y. Fu, J.Y. Zhang, J. Shi, W.M. Wang, H. Wang, Y.C. Wang, and Q.J. Zhang**: Nanocrystalline CoCrFeNiCuAl high-entropy solid solution synthesized by mechanical alloying. *J. Alloys Compd.* **485**, 34 (2009).

149. **K.B. Zhang, Z.Y. Fu, J.Y. Zhang, W.M. Wang, H. Wang, Y. C. Wang, and Q.J. Zhang**: Characterization of nanocrystalline CoCrFeNiCuAl high-entropy alloy powder processed by mechanical alloying. *Mater. Sci. Forum* **620–622**, 383 (2009).

150. **R. Sriharitha, B.S. Murty, and R.S. Kottada**: Phase formation in mechanically alloyed $Al_xCoCrCuFeNi$ (x = 0.45, 1, 2.5, 5 mol) high entropy alloys. *Intermetallics* **32**, 119 (2013).

151. **R. Sriharitha, B.S. Murty, and R.S. Kottada**: Alloying, thermal stability and strengthening in spark plasma sintered $Al_xCoCrCuFeNi$ high entropy alloys. *J. Alloys Compd.* **583**, 419 (2014).

152. **B. Niu, W. Ji, N. Li, F. Zhang, and Y. Wu**: Alloying and thermal behaviour of $CoCrFeNiMn_{0.5}Ti_{0.5}$ high-entropy alloy synthesised by mechanical alloying. *Mater. Sci. Technol.* **32**, 94 (2016).

153. **J. Wang, T. Guo, J. Li, W. Jia, and H. Kou**: Microstructure and mechanical properties of non-equilibrium solidified CoCrFeNi high entropy alloy. *Mater. Chem. Phys.* **210**, 192 (2018).

154. **J.M. Zhu, H.M. Fu, H.F. Zhang, A.M. Wang, H. Li, and Z. Q. Hu**: Microstructure and compressive properties of multiprincipal component $AlCoCrFeNiC_x$ alloys. *J. Alloys Compd.* **509**, 3476 (2011).

155. **Y. Zou, J.M. Wheeler, H. Ma, P. Okle, and R. Spolenak**: Nanocrystalline high-entropy alloys: A new paradigm in high-temperature strength and stability. *Nano Lett.* **17**, 1569 (2017).

156. **P. Yang, Y. Liu, X. Zhao, J. Cheng, and H. Li**: Electromagnetic wave absorption properties of $FeCoNiCrAl_{0.8}$ high entropy alloy powders and its amorphous structure prepared by high-energy ball milling. *J. Mater. Res.* **31**, 2398 (2016).

157. **J. Moon, Y. Qi, E. Tabachnikova, Y. Estrin, W.M. Choi, S. H. Joo, B.J. Lee, A. Podolskiy, M. Tikhonovsky, and H.S. Kim**: Deformation-induced phase transformation of $Co_{20}Cr_{26}Fe_{20}Mn_{20}Ni_{14}$ high-entropy alloy during high-pressure torsion at 77 K. *Mater. Lett.* **202**, 86 (2017).

158. **B. Schuh, B. Völker, V. Maier-Kiener, J. Todt, J. Li, and A. Hohenwarter**: Phase decomposition of a single-phase AlTiVNb high-entropy alloy after severe plastic deformation and annealing. *Adv. Eng. Mater.* **19**, 1 (2017).

159. **J. Čížek, P. Haušild, M. Cieslar, O. Melikhova, T. Vlasák, M. Janeček, R. Král, P. Harcuba, F. Lukáč, J. Zýka, and J. Málek**: Strength enhancement of high entropy alloy HfNbTaTiZr by severe plastic deformation. *J. Alloys Compd.* **553**, 316 (2018).

160. **W. Wu, S. Ni, Y. Liu, B. Liu, and M. Song**: Amorphization at twin-twin intersected region in FeCoCrNi high-entropy alloy subjected to high-pressure torsion. *Mater. Charact.* **127**, 111 (2017).

161. **A. Kilmametov, R. Kulagin, A. Mazilkin, S. Seils, T. Boll, M. Heilmaier, and H. Hahn**: High-pressure torsion driven mechanical alloying of CoCrFeMnNi high entropy alloy. *Scr. Mater.* **158**, 29 (2019).

162. **H. Shahmir, J. He, Z. Lu, M. Kawasaki, and T.G. Langdon**: Evidence for superplasticity in a CoCrFeNiMn high-entropy alloy processed by high-pressure torsion. *Mater. Sci. Eng., A* **685**, 342 (2017).

163. **H. Shahmir, T. Mousavi, J. He, Z. Lu, M. Kawasaki, and T. G. Langdon**: Microstructure and properties of a CoCrFeNiMn high-entropy alloy processed by equal-channel angular pressing. *Mater. Sci. Eng., A* **705**, 411 (2017).

164. **F.Y. Shu, S. Liu, H.Y. Zhao, W.X. He, S.H. Sui, J. Zhang, P. He, and B.S. Xu**: Structure and high-temperature property of amorphous composite coating synthesized by laser cladding FeCrCoNiSiB high-entropy alloy powder. *J. Alloys Compd.* **731**, 662 (2018).

https://doi.org/10.1557/jmr.2019.37 Published online by Cambridge University Press

© Materials Research Society 2019

165. **P. Yang, Y. Liu, X. Zhao, J. Cheng, and H. Li**: Electromagnetic wave absorption properties of mechanically alloyed FeCoNiCrAl high entropy alloy powders. *Adv. Powder Technol.* **27**, 1128 (2016).

166. **G. Zhu, Y. Liu, and J. Ye**: Fabrication and properties of Ti(C, N)-based cermets with multi-component AlCoCrFeNi high-entropy alloys binder. *Mater. Lett.* **113**, 80 (2013).

167. **Z. Tan, L. Wang, Y. Xue, P. Zhang, T. Cao, and X. Cheng**: High-entropy alloy particle reinforced Al-based amorphous alloy composite with ultrahigh strength prepared by spark plasma sintering. *Mater. Des.* **109**, 219 (2016).

168. **S. Yang, X. Yan, K. Yang, and Z. Fu**: Effect of the addition of nano-Al_2O_3 on the microstructure and mechanical properties of twinned $Al_{0.4}FeCrCoNi_{1.2}Ti_{0.3}$ alloys. *Vacuum* **131**, 69 (2016).

169. **K. Vasanthakumar, N.S. Karthiselva, N.M. Chawake, and S. R. Bakshi**: Formation of TiC_x during reactive spark plasma sintering of mechanically milled Ti/carbon nanotube mixtures. *J. Alloys Compd.* **709**, 829 (2017).

170. **W. Sun, X. Huang, and A.A. Luo**: Phase formations in low density high entropy alloys. *Calphad* **56**, 19 (2017).

171. **M. Vaidya, G. Mohan Muralikrishna, S.V. Divinski, and B. S. Murty**: Experimental assessment of the thermodynamic factor for diffusion in CoCrFeNi and CoCrFeMnNi high entropy alloys. *Scr. Mater.* **157**, 81 (2018).

172. **M. Vaidya, K.G. Pradeep, B.S. Murty, G. Wilde, and S. V. Divinski**: Bulk tracer diffusion in CoCrFeNi and CoCrFeMnNi high entropy alloys. *Acta Mater.* **146**, 211 (2018).

173. **S.V. Divinski, A. Pokoev, N. Esakkiraja, and A. Paul**: A mystery of "sluggish diffusion" in high-entropy alloys: The truth or a myth? arXiv preprint arXiv:1804.03465 (2018).

https://doi.org/10.1557/jmr.2019.37 Published online by Cambridge University Press

© Materials Research Society 2019